

System Identification and Stitched Modeling of the ADAPT™ Winged Compound Helicopter Scaled Demonstrator

Samuel J. Nadell
Aerospace Engineer
U.S. Army Combat Capabilities
Development Command
Aviation & Missile Center
Moffett Field, CA, USA

Tom Berger
Flight Controls Group Lead
U.S. Army Combat Capabilities
Development Command
Aviation & Missile Center
Moffett Field, CA, USA

Christopher DiMarco
Lead Research Engineer
Piasecki Aircraft Corporation
Essington, PA, USA

Mark J. S. Lopez
Flight Dynamics SME
U.S. Army Combat Capabilities
Development Command
Aviation & Missile Center
Moffett Field, CA, USA

ABSTRACT

Frequency-domain system identification was performed for the ADAPT™ Winged Compound Helicopter Scaled Demonstrator, a 10% scale version of the Piasecki X-49A, at four flight conditions spanning its flight envelope. Since the aircraft has eight redundant control effectors – lateral cyclic, longitudinal cyclic, collective, Vectored Thrust Ducted Propeller (VTDP) RPM, rudder, differential flaperon, symmetric flaperon, and elevator – and exhibits a large amount of inter-axis coupling, the Joint Input-Output (JIO) Method was used for system identification in addition to the Direct Method. Based on the identified frequency responses, a hybrid model structure, which explicitly includes the coupled fuselage-rotor flapping dynamics and a first-order model for VTDP RPM lag, was used. State-space models were identified at each flight condition, and combined with trim data to form a full flight envelope stitched simulation model. A detailed analysis of the trends of the stitched model trim, stability and control derivatives, eigenvalues, and frequency responses was performed.

NOTATION

CR	Cramér-Rao bound
D	Rotor diameter
$G_{\delta_1\delta_1}$	Primary control autospectrum
$G_{\delta_2\delta_2}$	Secondary control autospectrum
I	Insensitivity [%]
J_{ave}	Average frequency response cost
J_{rms}	RMS fit error (time-domain cost)
$L_{\beta_{1s}}$	Lateral rotor flap stiffness [s^{-2}]
M	Mixing matrix for control allocation
$M_{\beta_{1c}}$	Longitudinal rotor flap stiffness [s^{-2}]
N	Dynamic (Froude) scale factor
N	Mixing matrix for virtual effectors definition
p, q, r	Angular rates (roll, pitch, yaw)
r	Vector of reference inputs
s	Laplace-domain variable
TIC	Theil inequality coefficient (time-domain cost)
v	Vector of virtual effectors
y	Vector of aircraft responses
δ_A	Vector of individual actuators

$\gamma_{\delta_1\delta_2}^2$	Cross-control coherence
η	VTDP RPM lag state
τ_f	Rotor flap time constant [s]
ω_{lag}	VTDP RPM lag break frequency
ω_n	Natural frequency
ζ	Damping

INTRODUCTION

The Adaptive Digital Automated Pilotage Technology (ADAPT™) program, initiated by Piasecki Aircraft Corporation in 2014, has the goal of developing a flight control software that will achieve improvements in safety, survivability, performance, and affordability for Vertical Take-Off and Landing (VTOL) aircraft [1, 2]. ADAPT™ takes advantage of redundant control effectors, which are becoming increasingly common on modern VTOL platforms for applications such as Future Vertical Lift (FVL) and urban air mobility (UAM), by automatically allocating control to optimize performance during normal flight and re-allocating control in response to damage.

Previous work [2] involved development and piloted simulation of damage tolerant control laws using a simulated winged compound helicopter based on the Piasecki X-49A. The current effort, a follow-on collaboration between the U.S. Army Combat Capabilities Development Command Aviation & Missile Center (DEVCOM AvMC) and Piasecki, is focused on demonstrating ADAPT™ technology using a subscale flight-test vehicle based on the X-49A. The ADAPT™ Scaled Demonstrator program involves development of a stitched simulation model [3], control system, and damage tolerant control (DTC) for the full flight envelope. The work presented in this paper covers system identification at multiple flight conditions and stitched modeling of the Scaled Demonstrator, a first step in the larger effort.

Notably, this paper provides a useful case study for system identification of a winged compound helicopter using the Joint Input-Output (JIO) Method [4, 5], a post-processing step applied to the frequency-domain Direct Method [6] to account for highly correlated redundant control effectors, at multiple flight conditions. It will also further understanding of the configuration's flight dynamics through development of a stitched model and examination of the trends of trim, stability and control derivatives, eigenvalues, and frequency responses with airspeed.

The paper is organized as follows. First, a description of the Scaled Demonstrator flight vehicle is provided. Next, system identification methods and results are presented for two flight conditions and include the use of the JIO Method, state-space model structure selection, frequency-domain identification, and time-domain verification. Finally, a stitched model is generated using the identified point models and trim data. The stitched model trends are analyzed and implications for future work on DTC are discussed.

FLIGHT VEHICLE DESCRIPTION

The ADAPT™ Scaled Demonstrator is a 1:9.62 (approximately 10%) scale version of the Piasecki X-49A winged compound helicopter that leverages the bare airframe of the Align T-Rex 760 commercial RC helicopter, which has a semi-rigid two-bladed main rotor (no stabilizer bar), and was modified to more closely match the X-49A winged compound configuration. Figure 1 shows the two aircraft.

Modifications to the Align T-Rex 760 bare airframe include the addition of (1) carbon fiber wings with flaperons, (2) landing gear, and (3) a fully reconstructed tail. As shown in Figure 2, the reconstructed tail has elevons and a Vectored Thrust Ducted Propeller (VTDP), a primary feature of the X-49A, which consists of an aerodynamic duct, 13-in-diameter propeller, retractable sector, and rudder at the duct outlet. In hover, the sector is fully deflected to direct airflow in the starboard direction to oppose the torque of the clockwise-spinning main rotor. As airspeed increases, the sector is incrementally retracted to direct airflow along the aircraft's longitudinal axis to provide forward thrust; anti-torque is provided by lift forces on the rudder. The rudder and sector are mechanically linked; both are controlled by the same servo via the rudder/sector fulcrum. Figure 3 shows select

control positions scheduled with *beep*, a pilot control setting that is increased with airspeed.



Figure 1. ADAPT™ Scaled Demonstrator (left) and X-49A (right) [2].

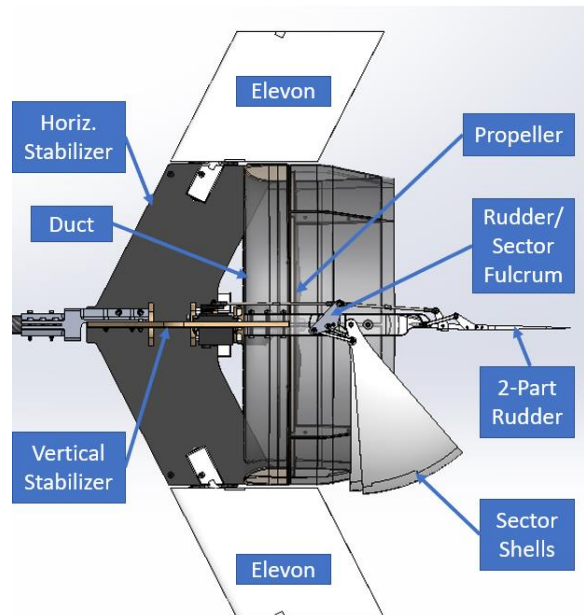


Figure 2. Vectored Thrust Ducted Propeller component diagram with retracted sector (top view).

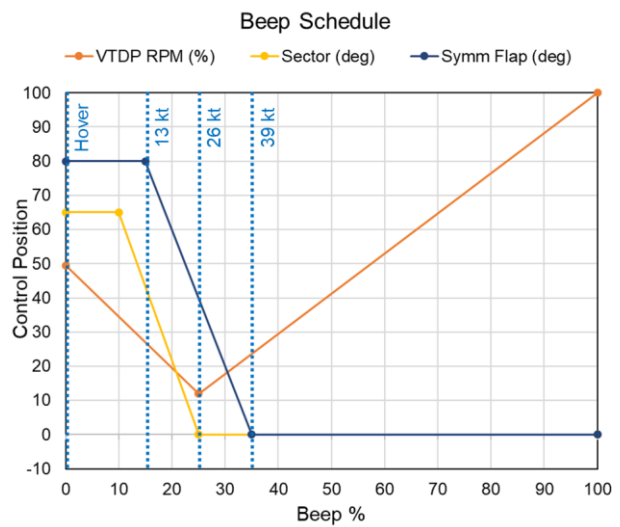


Figure 3. VTDP RPM, sector, and symmetric flaperon versus beep setting.

A key difference of the Scaled Demonstrator compared with the full-scale X-49A is that the VTDP propeller is controlled by RPM instead of collective pitch. RPM is a common control mechanism at subscale (e.g. in commercial multirotors) due to its lower complexity. However, collective pitch becomes a more effective option at full scale due to increasing rotor inertia and associated challenges for RPM control with (1) control response lag (i.e. the time required to speed up and slow down the rotor) and (2) drive system torque and power limits [9].

The Scaled Demonstrator has a takeoff weight of 37.65 lb and uses a Pixhawk 4 IMU for flight control. It uses Align DS820M swashplate servos, MKS HV6130H flaperon and elevon servos, and a Hitec HSB-9380TH servo for the rudder/sector.

In total, the Scaled Demonstrator has eight actuators, or bare-airframe inputs (shown in Table 1): left, right, and aft swashplate actuators; VTDP RPM; rudder; left and right flaperons; and left and right elevons, which were only actuated symmetrically and are considered herein as a single elevator input.

System identification guidelines for the Scaled Demonstrator were obtained by Froude scaling [7, 8] the full-scale guidelines given in [6]. The Froude scale factor N was determined as the ratio of the main rotor diameters of the Scaled Demonstrator (5.28 ft) and the X-49A (53.75 ft):

$$N = 9.62 \quad \text{Equation 1}$$

Challenges for system identification, which had to be addressed in this study, as well as flight control design, which will be addressed in future studies, for this configuration include: (1) scheduling control positions across all airspeeds, (2) highly coupled flight dynamics (particularly due to the VTDP), (3) reduced yaw authority during transition to forward flight as the rudder/sector rotates to align with the fuselage, and (4) decreasing control effectiveness of the aerosurfaces, and therefore control redundancy, with decreasing airspeed. These challenges also apply to the full-scale X-49A.

The following section discusses the point model identification methodology, and how some of the system identification challenges were addressed.

POINT MODEL IDENTIFICATION METHODOLOGY

Overview of the JIO Method

Determining the aircraft response to each actuator (y/δ_A) is important for determining control allocation for future work on damage tolerant control (DTC). Frequency-domain system identification typically proceeds by exciting the system with piloted or automated inputs (e.g. frequency sweeps), measuring the individual actuator and aircraft responses, and then using the measured time history data to identify bare-airframe frequency responses using the Direct Method [6].

The Direct Method can be used when the average cross-control coherence between the primary input δ_1 and each secondary input δ_2 is [6]:

$$(\gamma_{\delta_1\delta_2}^2)_{\text{ave}} < 0.5 \quad \text{Equation 2}$$

If the above condition is not met, the Direct Method may still be used if all secondary control autospectra are small compared to the primary control autospectrum [6]:

$$(G_{\delta_2\delta_2})_{\text{ave}} \leq (G_{\delta_1\delta_1})_{\text{ave}} - 20 \text{ dB} \quad \text{Equation 3}$$

If neither of the conditions in Equations 2 and 3 are met, then the JIO Method must be used [4].

For some responses, the Scaled Demonstrator requires using the Joint-Input Output (JIO) Method [4, 5] due to high cross-control correlations resulting from closed-loop system identification, highly coupled flight dynamics, and highly correlated redundant control effectors. The JIO Method requires measurement of the external excitations, referred to as the reference inputs r , in addition to the individual actuator responses δ_A and aircraft responses y . Using the JIO Method, the matrix of bare-airframe frequency responses to the individual actuator inputs (y/δ_A) can be determined from the matrix of bare-airframe frequency responses to the reference inputs (y/r) and individual actuator frequency responses to the reference inputs (δ_A/r) as follows [4]:

$$\begin{bmatrix} y \\ \delta_A \end{bmatrix} = \begin{bmatrix} y \\ r \end{bmatrix} \begin{bmatrix} \delta_A \\ r \end{bmatrix}^{-1} \quad \text{Equation 4}$$

For the single-input single-output case, the JIO Method can be thought of as a ‘‘chain-rule’’ type of expansion. The JIO Method uses two intermediate Direct Method calculations (one for y/r and another for δ_A/r) and a matrix multiplication, and therefore can be thought of as a post-processing extension to the Direct Method.

It is advantageous to define reference inputs r that will excite symmetric and differential *groups* of actuators via a mixing matrix M (as shown in Figure 4) to concentrate the vehicle response to a primary axis, which will result in higher signal-to-noise ratio and coherence during identification [5].

Virtual effectors v can be defined by grouping, or ganging, the individual actuators δ_A via a mixing matrix N (as shown in Figure 4), which is typically set to $N = M^{-1}$ [5]. The virtual effectors capture the responses of the groups of actuators to the corresponding reference inputs (v/r), which can in turn be used to obtain the aircraft responses to the groups of actuators (y/v) via the JIO Method. The equivalent JIO Method equation using virtual effectors v instead of individual actuators δ_A is:

$$\begin{bmatrix} y \\ v \end{bmatrix} = \begin{bmatrix} y \\ r \end{bmatrix} \begin{bmatrix} v \\ r \end{bmatrix}^{-1} \quad \text{Equation 5}$$

Figure 4 shows a notional block diagram with the key signals used for identification using the JIO Method. The block diagram elements are as follows: M is a mixing matrix used

to allocate the reference signals to the individual actuators, N is a mixing matrix that defines the relationship between the virtual effectors and individual actuators, C represents the control system, and H represents the sensors.

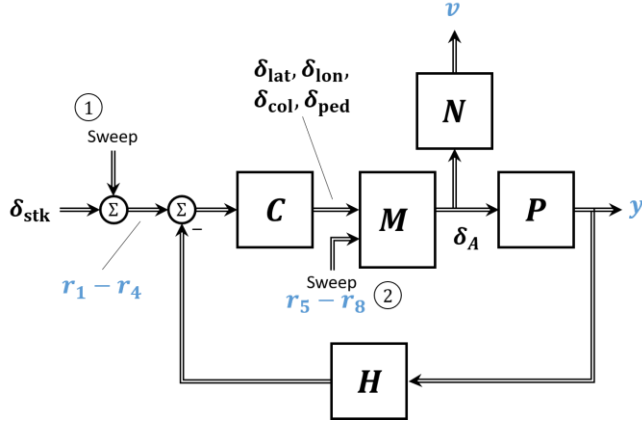


Figure 4. Block diagram showing the locations of the reference input frequency sweeps and other key signals required for the JIO Method.

Table 1 defines the reference inputs, virtual effectors, and individual actuators used in this study and shown in Figure 4. Although the aircraft response to each individual actuator is desired, reference inputs and virtual effectors are used in the analysis to concentrate vehicle excitations to a particular axis. Note that although the name “VTDP RPM” is used for reference input r_5 , virtual effector v_4 , and actuator input δ_{rpm} , the signals are actually in units of PWM and not RPM. The term “RPM” is used here because these signals are treated as a surrogate for the VTDP speed.

Table 1. Key Signals for System Identification

Reference Inputs (r)	Virtual Effectors (v)	Individual Actuators (δ_A)
Pilot Lateral Cyclic (r_1)	Lateral Cyclic (v_1)	Left Swashplate (δ_{spl})
Pilot Lon. Cyclic (r_2)	Longitudinal Cyclic (v_2)	Right Swash. (δ_{spr})
Pilot Collective (r_3)	Collective (v_3)	Aft Swashplate (δ_{spa})
Pilot Pedal (r_4)	VTDP RPM (v_4)	VTDP RPM (δ_{rpm})
VTDP RPM (r_5)	Rudder (v_5)	Rudder (δ_r)
Differential Flaperon (r_6)	Differential Flaperon (v_6)	Left Flaperon (δ_{fl})
Symmetric Flaperon (r_7)	Symmetric Flaperon (v_7)	Right Flaperon (δ_{fr})
Elevator (r_8)	Elevator (v_8)	Elevator (δ_e)

Description of Reference Inputs

As described in [5], the external reference input frequency sweeps can be injected (1) into the tracking command (i.e. pilot stick) path (marked 1 in Figure 4) or (2) directly into the actuators via a mixing matrix M (marked 2 in Figure 4), which is designed to excite groups of actuators and concentrate the aircraft response to one primary axis. In this study, the mixing matrix M is given by:

$$M = \begin{bmatrix} \delta_{spl} \\ \delta_{spr} \\ \delta_{spa} \\ \delta_{rpm} \\ \delta_r \\ \delta_{fl} \\ \delta_{fr} \\ \delta_e \end{bmatrix} = \begin{bmatrix} -0.866 & -0.5 & 1 \\ 0.866 & -0.5 & 1 \\ 0 & 1 & 1 \\ & & a & 1 \\ & & & b \\ & & & & 1 & 1 \\ & & & & -1 & 1 \\ & & & & & & 1 \end{bmatrix} \begin{bmatrix} \delta_{lat} \\ \delta_{lon} \\ \delta_{col} \\ \delta_{ped} \\ r_5 \\ r_6 \\ r_7 \\ r_8 \end{bmatrix}$$

Equation 6

In the mixing matrix M above, constants a and b represent the changes in the pilot pedal (yaw) control mode with airspeed. Figure 5 below shows how a and b vary with airspeed. At hover, $a = 1$ and $b = 0$ such that pilot pedal (r_4) excites VTDP RPM (δ_{rpm}). At 13 kt, r_4 excitation is split between δ_{rpm} and rudder δ_r . At 26 and 39 kt, $a = 0$ and $b = 1$ such that pilot pedal (r_4) excites δ_r only.

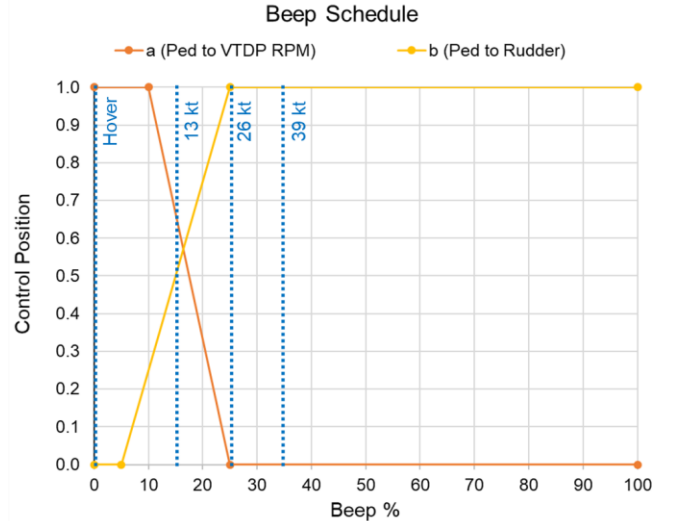


Figure 5. The pilot yaw control mode is scheduled with beep such that pedal primarily controls VTDP RPM at low speed and rudder at high speed.

The tracking command sweeps (r_1 - r_4 in Figure 4) are passed through control system channels δ_{lat} , δ_{lon} , δ_{col} , δ_{ped} and since the control system for this aircraft only operates through the swashplate servos, VTDP RPM (for low-speed yaw control), and rudder (for high-speed yaw control), only those effectors can be excited through this method. Therefore, tracking command sweeps were supplemented by direct

actuator sweeps (r_5 - r_8 in Figure 4) to excite the redundant effectors (flaperons and elevator) that were not accessible via the tracking command path. However, a potential disadvantage of closed-loop direct actuator sweeps is that they appear as a disturbance to the control system, which suppresses the aircraft responses [5]. This may result in reduced aircraft response and therefore lower signal-to-noise ratio and coherence, which was observed in this study, particularly at low frequency (where the control system is active).

Note that, at hover and 13 kt, reference inputs r_5 - r_8 were not used since the frequency sweeps of the aerosurfaces did not excite sufficient aircraft response for system identification. At 26 and 39 kt, since $a = 0$, the r_5 reference input *must* be used to excite the VTDP RPM actuator directly.

Description of Virtual Effectors

As previously described, the measurements of the individual actuators δ_A were grouped into virtual effectors \mathbf{v} via a mixing matrix \mathbf{N} , which provides an intuitive understanding of the effect the actuators will have on a primary axis of aircraft response [5]. In this study, the virtual effectors were defined relative to the individual actuators as $\mathbf{v} = \mathbf{N}\delta_A$ where mixing matrix \mathbf{N} is based on the inverse of \mathbf{M} , and is given by:

$$\begin{bmatrix} v_1 \\ v_2 \\ v_3 \\ v_4 \\ v_5 \\ v_6 \\ v_7 \\ v_8 \end{bmatrix} = \underbrace{\begin{bmatrix} -0.577 & 0.577 & 1 & & & & & \\ -0.333 & -0.333 & 0.667 & & & & & \\ 0.333 & 0.333 & 0.333 & & & & & \\ & & & 1 & & & & \\ & & & & 1 & & & \\ & & & & & 0.5 & -0.5 & \\ & & & & & 0.5 & 0.5 & \\ & & & & & & & 1 \end{bmatrix}}_{\mathbf{N}} \begin{bmatrix} \delta_{spl} \\ \delta_{spr} \\ \delta_{spa} \\ \delta_{rpm} \\ \delta_r \\ \delta_{fl} \\ \delta_{fr} \\ \delta_e \end{bmatrix}$$

Equation 7

Virtual effectors v_4 and v_5 are set equal to δ_{rpm} and δ_r such that mixing matrix \mathbf{N} is constant for all flight conditions.

FLIGHT TEST OVERVIEW

As shown in Table 2, flight testing was performed at hover, 13, 26, and 39 kt and included reference input sweeps to identify frequency responses, doublets for time-domain verification, and static stability tests to improve the accuracy of low-frequency speed derivatives such as M_u at each flight condition. The 13 kt increment was selected by Froude scaling the guideline in [6], which states that full-scale point models should be identified at a spacing of 40 kt to cover the flight envelope. Each frequency sweep was automated and performed three times to ensure sufficient data were obtained for system identification. Piloted doublet maneuvers were performed twice (once in each direction) to verify the models in the time domain.

Table 3 summarizes frequency sweep settings used during flight testing. The frequency sweeps were automated using the function in [6] over a prescribed range of $\omega = 0.6$ -50 rad/s to excite the aircraft dynamics, which occur at higher frequency than at full scale. Since frequency Froude scales as $1/\sqrt{N}$, this range corresponds to 0.2-16 rad/s at full scale, which fully covers the typical full-scale range of 0.3-12 rad/s given in [6]. Five seconds of trim were collected at the beginning and end of each frequency sweep.

Table 2. System Identification Flight Tests

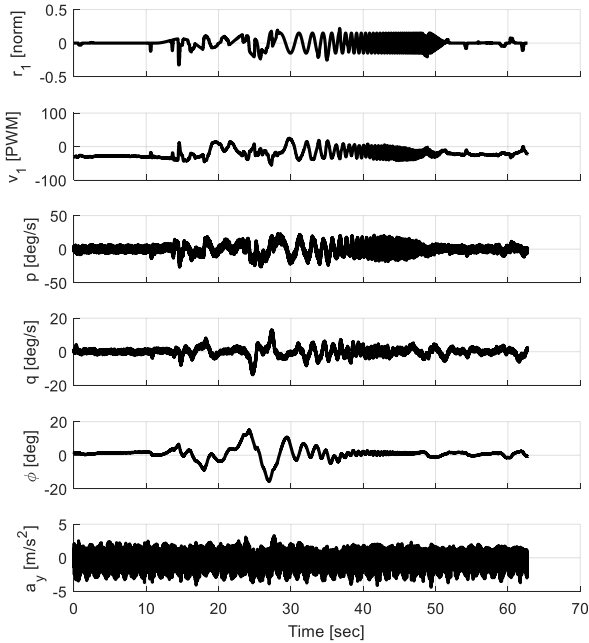
Maneuver	Flight Conditions
Pilot Lat Freq. Sweep (3)	All
Pilot Lon Freq. Sweep (3)	All
Pilot Col Freq. Sweep (3)	All
Pilot Ped Freq. Sweep (3)	All
VTDP RPM Freq. Sweep (3)	26, 39 kt
Diff Flap Freq. Sweep (3)	26, 39 kt
Symm Flap Freq. Sweep (3)	26, 39 kt
Elevator Freq. Sweep (3)	26, 39 kt
Pilot Lat Doublet (2*)	All
Pilot Lon Doublet (2*)	All
Pilot Col Doublet (2*)	All
Pilot Ped Doublet (2*)	All
Longitudinal Static Stability (1)	All
Lateral Static Stability (1)	Hover only
Steady Heading Sideslip (1)	Forward flight only

*In both directions (e.g. left/right, right/left)

Table 3. Frequency Sweep Settings

Frequency Sweep Setting	Value
Minimum frequency ω_{\min} [rad/s]	0.6
Maximum frequency ω_{\max} [rad/s]	50.0
Sweep length T_{rec} [sec]	50.0
Start and end trimtime T_{trim} [sec]	5.0
Fade-in time $T_{\text{f,in}}$ [sec]	7.0
Fade-out time $T_{\text{f,out}}$ [sec]	2.0
Low-frequency dwell time T_{park} [sec]	10.0

Frequency sweep amplitudes were selected to produce sufficient aircraft responses for system identification. Roll, pitch, and yaw rates of ± 25 deg/s and heave accelerations of ± 3 m/s² (± 8 deg/s and ± 3 m/s² full scale, respectively) were found to be sufficient for system identification in hover and are consistent with the full-scale guidelines [6]. In addition to flight testing in calm weather (no wind), these response amplitudes help ensure sufficient signal-to-noise ratios and coherences to identify frequency responses. Figure 6 shows the key signals during a lateral cyclic (r_l) reference input frequency sweep in hover as an example.

**Figure 6. Frequency sweep of the r_l reference input in hover.**

POINT MODEL IDENTIFICATION RESULTS

This section presents the model structure used for system identification and the identification results at hover and 26 kt. It will cover special considerations for system identification at each flight condition, frequency-domain identification results, and time-domain verification results.

Model Structure

Based on the identified frequency responses, a hybrid model structure was selected to extend the six-degree-of-freedom (6DOF) model and explicitly include the coupled fuselage-rotor flapping dynamics [6]. Previous work [8, 10, 11] used a first-order actuator model to represent the lag associated with an electric motor. In this work, a first-order actuator model with break frequency ω_{lag} was similarly added to the model structure to represent the lag associated with the VTDP RPM v_4 control inputs. The equations of motion as implemented in CIFER[®] are given by:

$$\begin{aligned}
 \dot{u} &= X_u u + X_w w + (X_q - W_0)q + (X_r + V_0)r \\
 &\quad - (g \cos \theta_0)\theta + X_{\beta_{1c}} \beta_{1c} + X_\eta \eta + X_{v_3} v_3 \\
 &\quad + X_{v_7} v_7 + X_{v_8} v_8 \\
 \dot{v} &= Y_u u + Y_v v + (Y_p + W_0)p + (Y_r - U_0)r + (g \cos \theta_0)\phi \\
 &\quad + Y_{\beta_{1s}} \beta_{1s} + Y_\eta \eta + Y_{v_5} v_5 + Y_{v_6} v_6 \\
 \dot{w} &= Z_w w - V_0 p + (Z_q + U_0)q - (g \sin \theta_0)\theta + Z_{v_2} v_2 \\
 &\quad + Z_{v_3} v_3 + Z_{v_7} v_7 + Z_{v_8} v_8 \\
 \dot{p} &= L_u u + L_v v + L_{\beta_{1s}} \beta_{1s} + L_{v_3} v_3 + L_{v_5} v_5 + L_{v_6} v_6 \\
 \dot{q} &= M_u u + M_v v + M_{\beta_{1c}} \beta_{1c} + M_{v_3} v_3 + M_{v_7} v_7 + M_{v_8} v_8 \\
 \dot{r} &= N_u u + N_w w + N_r r + N_\eta \eta + N_{v_3} v_3 + N_{v_5} v_5 + N_{v_6} v_6 \\
 \phi &= p \\
 \dot{\theta} &= q \\
 \tau_f \dot{\beta}_{1c} &= \tau_f q - \beta_{1c} + M f_{\beta_{1s}} \beta_{1s} + M f_{v_1} v_1 + M f_{v_2} v_2 \\
 \tau_f \dot{\beta}_{1s} &= \tau_f p - \beta_{1s} + L f_{\beta_{1c}} \beta_{1c} + L f_{v_1} v_1 + L f_{v_2} v_2 \\
 \dot{\eta} &= -\omega_{\text{lag}} \eta + \omega_{\text{lag}} v_4
 \end{aligned}$$

Equation 8

Input time delay terms are also included in the identified model, but are omitted from Equation 8 for simplicity.

For system identification, the trim terms were determined as follows: $U_0 \approx V_T$ is approximated from the known flight condition (0, 13, 26, 39 kt), θ_0 is measured, $\Phi_0 = 0$, $V_0 = 0$, and $W_0 = V_T \sin \theta_0$ (enforcing level flight). The body-axis accelerations are reconstructed from accelerometer measurements for use in the model identification:

$$\begin{aligned}
 \dot{u} &= a_x - W_0 q + V_0 r - (g \cos \theta_0)\theta \\
 \dot{v} &= a_y + W_0 p - U_0 r + (g \cos \theta_0)\phi \\
 \dot{w} &= a_z - V_0 p + U_0 q - (g \sin \theta_0)\theta
 \end{aligned}$$

Equation 9

The aircraft responses have units of m/s², rad/s, and rad and the virtual effectors have units of PWM. Model parameters (stability and control derivatives in Equation 8) were identified in CIFER[®] to minimize the cost of the mismatch between the model and flight-data frequency responses.

Notably, control derivatives associated with the aerosurfaces – rudder (v_5), differential flaperon (v_6), symmetric flaperon (v_7), and elevator (v_8) – were dropped from the model structure at hover and 13 kt since frequency sweeps of the aerosurfaces did not excite sufficient aircraft response (and associated signal-to-noise ratio) for system identification. The aerosurface control derivatives are included in the model structure at 26 and 39 kt where aerosurface lift forces are sufficiently effective to identify responses.

Note that the aircraft response to each individual actuator (y/δ_A) can ultimately be obtained by converting the B matrix of the identified state-space model, which is in terms of virtual effectors, to being in terms of the individual actuators. This is accomplished by multiplying the B matrix by the mixing matrix N :

$$B_{\delta_A} = B_v N \quad \text{Equation 10}$$

Frequency-Domain System Identification and Time-Domain Verification at Hover

As previously discussed, identification using the JIO Method is required when virtual effectors exhibit high cross-control correlations. An example of this was the high cross-control correlation between the longitudinal cyclic v_2 and the lateral cyclic v_1 during the pitch r_2 sweeps at hover as shown in Figure 7. The high cross-control correlation for this virtual effector is due to high pitch-roll coupling; the resulting roll response to pitch inputs is fed back to lateral cyclic v_1 through the control system during closed-loop system identification. The JIO Method is required here since the average cross-control correlation is greater than 0.5 and the secondary control autospectrum ($G_{v_1 v_1}$) is within 20 dB of the primary control autospectrum ($G_{v_2 v_2}$). In this case, however, collective v_3 and VTDP RPM v_4 had low coherences, and could be ignored in the JIO formulation. Therefore, a JIO case was set up using only lateral cyclic v_1 and longitudinal cyclic v_2 (labeled Case A in Table 4). Similarly, a second JIO case was setup (Case B) for collective v_3 and VTDP RPM v_4 , which were highly correlated during the pilot collective r_3 and pilot pedal r_4 sweeps. The selection of JIO Case B or Direct Method for the v_3 and v_4 frequency responses (as listed in Table 5), will be discussed further in a later section.

Table 4 lists the frequency response generation methods (Direct and JIO Method cases) used for system identification at hover. Table 5 lists the method used for each frequency response.

Table 4. Freq. Response Generation Methods at Hover

Method	Sweep Type	Identified Effector Responses
Direct Method	Ref. input (r) corresponding to effector (v) only	Virtual effector (v) of interest only
JIO Case A	Pilot Lat Cyclic (r_1) Pilot Lon Cyclic (r_2)	Lat Cyclic (v_1) Lon Cyclic (v_2)
JIO Case B	Pilot Collective (r_3) Pilot Pedal (r_4)	Collective (v_3) VTDP RPM (v_4)

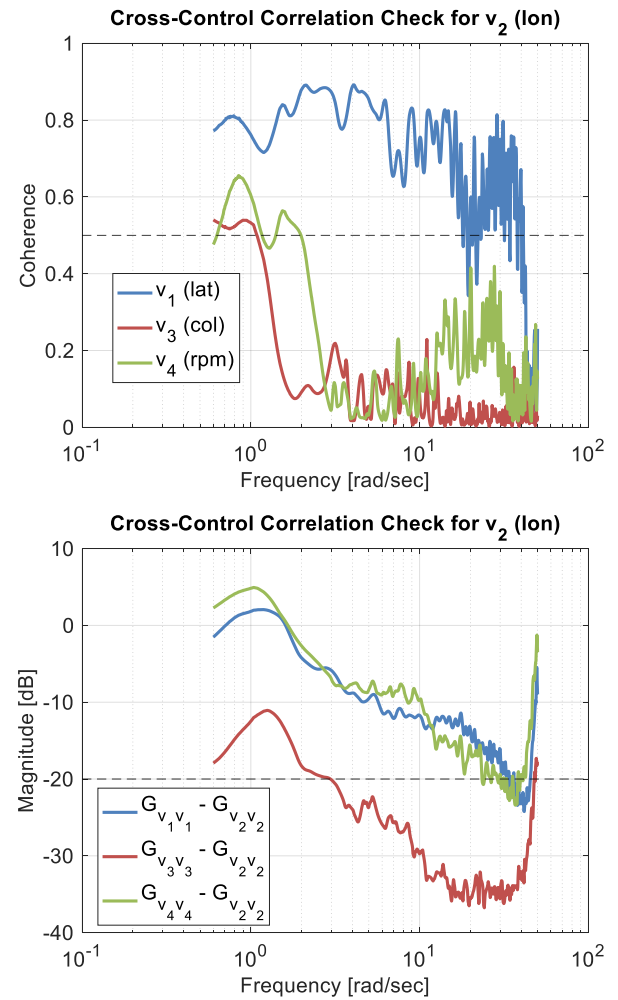


Figure 7. The longitudinal cyclic virtual effector (v_2) has high cross-control correlation with the lateral cyclic virtual effector (v_1).

Table 5. Method Used for Each Freq. Response at Hover

Response	Method
\dot{v}/v_1	JIO Case A
p/v_1	JIO Case A
q/v_1	JIO Case A
a_y/v_1	JIO Case A
\dot{u}/v_2	JIO Case A
p/v_2	JIO Case A
q/v_2	JIO Case A
a_x/v_2	JIO Case A
\dot{w}/v_3	Direct Method
r/v_3	JIO Case B
a_z/v_3	Direct Method
\dot{u}/v_4	Direct Method
\dot{v}/v_4	Direct Method
r/v_4	Direct Method
a_x/v_4	Direct Method
a_y/v_4	Direct Method

As is common for single main rotor helicopters, in this study it was difficult to achieve satisfactory coherence at low frequency due to low signal-to-noise ratio and high cross-control correlations at low frequency [6]. Although there was sufficient data to identify X_u with good precision (as shown later in Table 7), the speed-stability derivative M_u had a large insensitivity value. Therefore, M_u was calculated and fixed during state-space model identification using an alternative approach [6]. First, a preliminary full-order state-space model was obtained from system identification at hover. Next, the bare-airframe model was reduced to the rigid-body six-degree-of-freedom (6DOF) quasi-steady dynamics by eliminating the higher-order flapping states β_{1c}, β_{1s} . The 6DOF form of the pitch equation of motion is given by:

$$\dot{q} = M_{u,\text{eff}}u + M_{v,\text{eff}}v + M_{v_1,\text{eff}}v_1 + M_{v_2,\text{eff}}v_2 \quad \text{Equation 11}$$

In trimmed hover flight, pitch acceleration \dot{q} and body-axis velocity v are zero. Solving gives an equation for M_u

$$M_u = -[M_{v_1,\text{eff}} \frac{\Delta v_1}{\Delta u} + M_{v_2,\text{eff}} \frac{\Delta v_2}{\Delta u}] \quad \text{Equation 12}$$

in terms of trim gradients, which were obtained from static stability data, and known 6DOF derivatives. An analogous approach was applied during system identification at the other flight conditions.

The resulting hover model has an average frequency-domain cost of $J_{\text{ave}} = 52$, which meets the guideline of $J_{\text{ave}} < 100$ given in [6] and indicates very good agreement between the model and flight data.

Figure 8 shows on-axis frequency responses identified for the Scaled Demonstrator at hover. The on-axis p/v_1 response exhibits a coupled lateral fuselage-rotor flapping mode at high frequency that is well captured by the hybrid model structure. The equations below provide the SISO approximation of the

mode natural frequency and damping from the identified parameters, which provide physical intuition [6]:

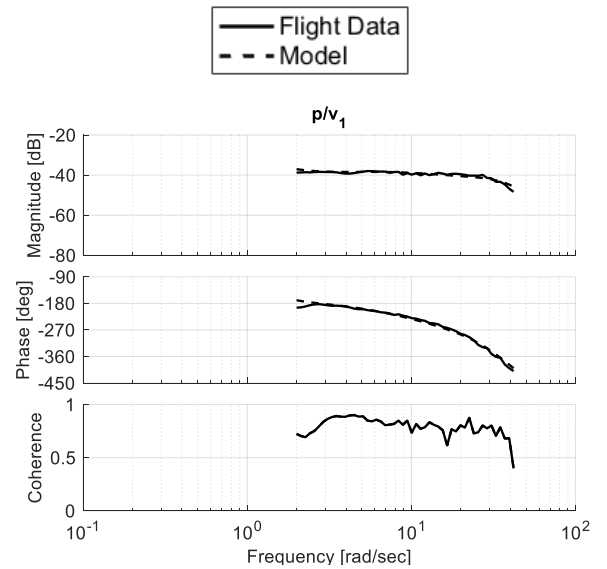
$$\omega_n \approx \sqrt{-L_{\beta_{1s}}} \quad \text{Equation 13}$$

$$\zeta \approx \frac{1}{2\omega_n\tau_f} \quad \text{Equation 14}$$

Therefore, the identified values $L_{\beta_{1s}} = -785.236 \text{ s}^{-2}$ and $\tau_f = 0.039 \text{ s}$ (shown later in Table 7) are primary contributors in the resulting natural frequency and damping of $\omega_n = 36.1 \text{ rad/s}$ and $\zeta = 0.49$ obtained from the MIMO system eigenvalues.

The longitudinal coupled fuselage-rotor flapping mode has an identified longitudinal flap stiffness $M_{\beta_{1c}} = -104.638 \text{ s}^{-2}$ (shown later in Table 7). The natural frequency and damping obtained from the MIMO system eigenvalues are $\omega_n = 8.1 \text{ rad/s}$ and $\zeta = 0.99$. The lower frequency and higher damping is evident in the on-axis q/v_2 response of Figure 8, which rolls off at lower frequency than the corresponding lateral flapping mode.

The terms $L_{\beta_{1s}}$ and $M_{\beta_{1c}}$ represent the rotor flap stiffnesses. The stiffnesses are *relative* to the roll and pitch inertias, respectively, thus the ratio of the *roll to pitch* rotor flap stiffness of 7.5 represents the ratio of the *pitch to roll* moment of inertia [6]. That is, the magnitude of $L_{\beta_{1s}}$ is much larger than that of $M_{\beta_{1c}}$ since the aircraft's roll inertia is much smaller than its pitch inertia (both of which are typical).



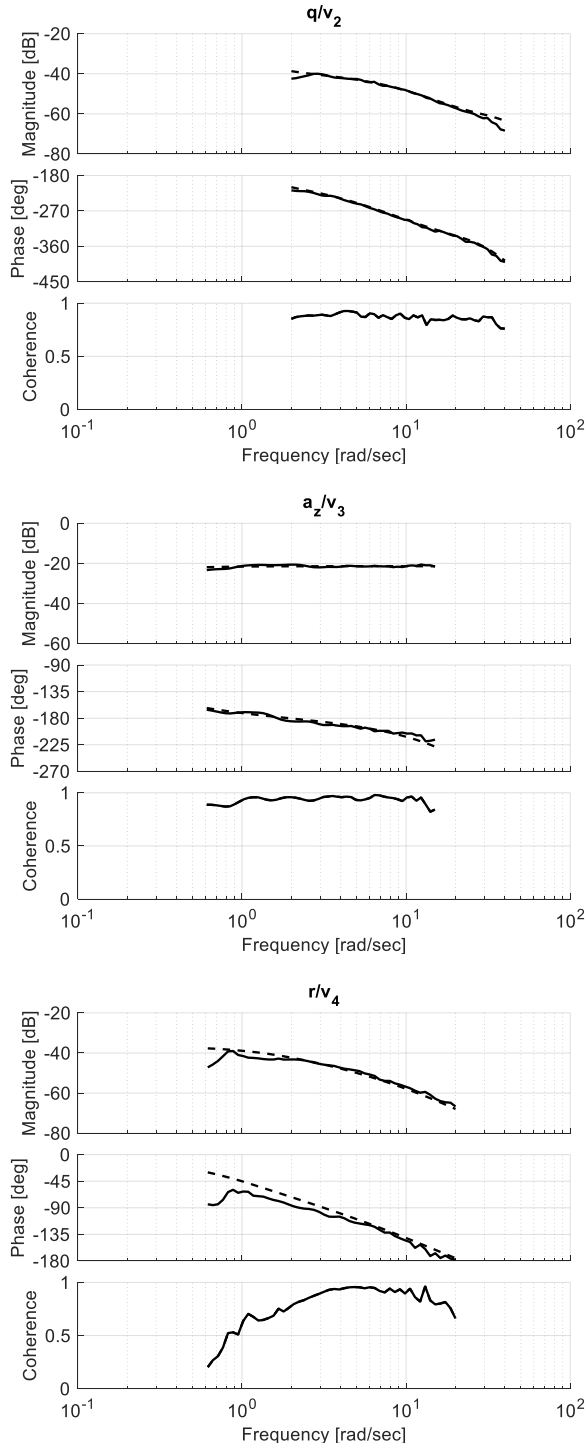


Figure 8. On-axis frequency responses identified at hover.

As shown in Figure 9, the off-axis p/v_2 response has a relatively large magnitude (-51 dB at 10 rad/s) compared to the on-axis q/v_2 response (-49 dB at 10 rad/s), which indicates significant pitch-roll coupling. The off-axis q/v_1 response is also present, but has a smaller magnitude (-56 dB at 10 rad/s) compared to the on-axis p/v_1 response (-39 dB at 10 rad/s). This indicates that roll-pitch coupling is also present, but to a smaller degree than pitch-roll coupling, which is also typical

at full scale [6]. Discussion with the Piasecki test pilot and flight-test team confirmed these observations qualitatively during flight testing. It was noted that the highly coupled pitch-roll and roll-pitch dynamics may be due to the design of the swashplate phase offset, which could be optimized to reduce this cross-coupling. Additionally, the high rotor stiffness described by flap stiffness terms $L_{\beta_{1s}}$ and $M_{\beta_{1c}}$ is also a primary factor contributing to pitch-roll and roll-pitch coupling [6]. In Equation 8, the rotor flap *control* coupling terms Lf_{v_2} and Mf_{v_1} are inter-axis coupling terms due to the control inputs; the rotor flap *response* coupling terms $Lf_{\beta_{1c}}$ and $Mf_{\beta_{1s}}$ are inter-axis coupling terms due to the state responses. These terms capture the coupled dynamics: Lf_{v_2} and $Lf_{\beta_{1c}}$ for pitch-roll coupling and Mf_{v_1} and $Mf_{\beta_{1s}}$ for roll-pitch coupling. The cross-coupled rotor flap responses are transmitted to the fuselage to produce pitch and roll moments via the large rotor flap stiffness terms $L_{\beta_{1s}}$ and $M_{\beta_{1c}}$.

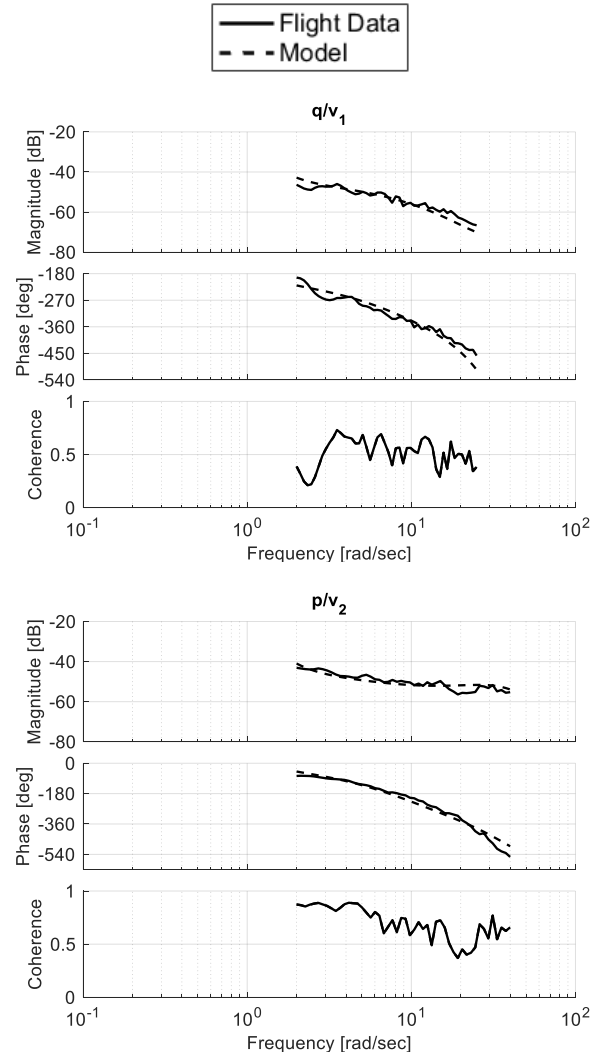


Figure 9. Off-axis q/v_1 and p/v_2 responses at hover.

Figure 10 demonstrates the importance of the first-order VTDP RPM lag model in matching the high-frequency roll-off in the r/v_4 response exhibited by the flight data. The figure overlays the final state-space model (green line), which

includes a model for VTDP RPM lag, compared with a preliminary model (red line) that does not. As given in Equation 8, the VTDP RPM lag model is first-order and represents the lag associated with speeding up and slowing down the VTDP propeller. The identified parameter $\omega_{\text{lag}} = 9.7$ rad/s is the motor lag break frequency, which effectively sets the bandwidth of the aircraft response to the VTDP RPM virtual effector and introduces lag to the system above this frequency.

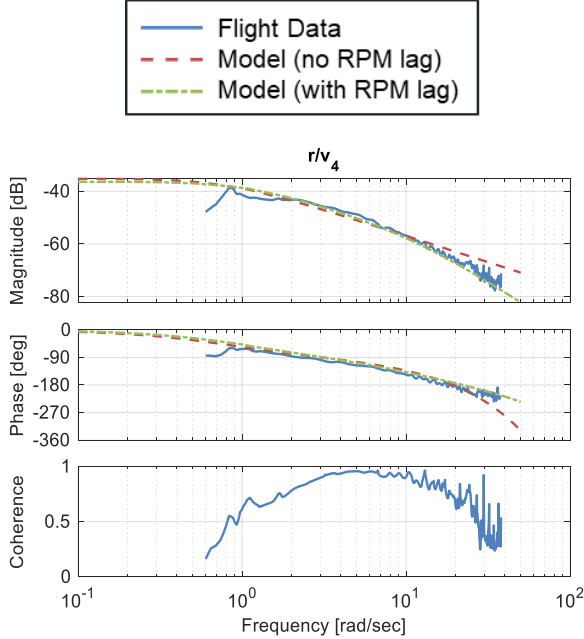


Figure 10. Addition of a first-order VTDP RPM lag model improves the match with the high-frequency roll-off exhibited by the flight data.

Table 6 shows costs associated with each frequency response. Overall, on-axis frequency response mismatch costs, as well as the average mismatch cost, are low indicating a good model accuracy. Table 7 shows the identified parameters and the associated Cramér-Rao bounds (CR) and insensitivities (I) [6]. All identified parameters are known to good accuracy and not correlated with any other parameters as indicated by their low insensitivity ($I < 10\%$) and Cramér-Rao bound ($CR < 20\%$) values.

Figure 11 shows time-domain verification results for a piloted lateral doublet at hover. For a full-scale aircraft, the time-domain cost guidelines for an acceptable model are RMS fit error $J_{\text{rms}} < 2.0$ and normalized Theil inequality coefficient (TIC) < 0.3 [6]. In previous work [12], the RMS fit error guideline was Froude scaled by \sqrt{N} for subscale aircraft. Examination of scale factors corresponding to each aircraft response indicates that this scale factor is primarily attributed to the angular rates, which scale as \sqrt{N} , whereas accelerations and attitudes scale directly (i.e. have a scale factor of 1) [7]. Thus, the Froude-scaled RMS fit error guideline for the Scaled Demonstrator is $J_{\text{rms,Fr}} < 6.2$. As shown in Table 8, the costs meet the $J_{\text{rms,Fr}}$ and TIC guidelines, indicating good agreement between the model and flight data.

Table 6. Frequency Response Costs at Hover

Response	Cost	Freq. [rad/s]
\dot{v}/v_1	16.8	2.0-30
p/v_1	20.0	2.0-42
q/v_1	80.0	2.0-25
a_y/v_1	19.5	2.0-30
\dot{u}/v_2	120.0	2.0-40
p/v_2	142.7	2.0-40
q/v_2	39.2	2.0-40
a_x/v_2	134.3	2.0-40
\dot{w}/v_3	9.7	0.6-10
r/v_3	29.2	1.0-30
a_z/v_3	11.7	0.6-15
\dot{u}/v_4	20.8	2.0-25
\dot{v}/v_4	50.5	2.0-20
r/v_4	72.9	0.6-20
a_x/v_4	46.1	0.6-20
a_y/v_4	20.0	1.2-20
J_{ave}	52.1	-

Table 7. Parameters Identified at Hover

Parameter	Value	CR (%)	I (%)
τ_f	0.039194	6.6	0.9
X_u	-0.35055	10.2	4.8
X_r	0 ^b	-	-
$X_{\beta_{1c}}$	15.3552	6.3	0.6
X_η	0.0038095	3.7	1.4
Y_v	-0.16244 ^c	-	-
Y_p	0.26005	14.7	6.3
Y_r	0.22462	14.8	5.9
$Y_{\beta_{1s}}$	$-X_{\beta_{1c}}$ ^a	-	-
Y_η	-0.0037048	4.4	1.5
Z_w	-0.21254	22.7	10.9
L_u	0 ^b	-	-
L_v	-3.3457	16.4	5.7
$L_{\beta_{1s}}$	-785.1572	7.8	1.5
M_u	0.51103 ^c	-	-
M_v	0.22179	22.7	8.8
$M_{\beta_{1c}}$	-104.569	6.4	0.6
N_w	0.49168	14.5	6.4
N_r	-1.2677	12.4	4.6
N_η	0.018457	5.4	2.0
$Mf_{\beta_{1s}}$	-0.89057	10.0	3.0
$Lf_{\beta_{1c}}$	0.65726	6.4	1.3
ω_{lag}	9.684	7.3	1.9
Z_{v_3}	-0.08505	2.7	1.3
N_{v_3}	-0.0079331	12	5.8
Mf_{v_1}	0.00016509	9.5	2.7
Mf_{v_2}	0.00037684	7.1	1.0
Lf_{v_1}	0.00033729	7.0	1.5
Lf_{v_2}	-0.00014599	8.8	2.0
τ_{v_1}	0.038648	8.0	2.5
τ_{v_2}	0.033918	7.2	2.3

Parameter	Value	CR (%)	I (%)
τ_{v_3}	0.056975	8.8	4.1
τ_{v_4}	0.021695	16.5	5.8

^a Constrained parameter

^b Eliminated parameter from model structure

^c Fixed parameter in model

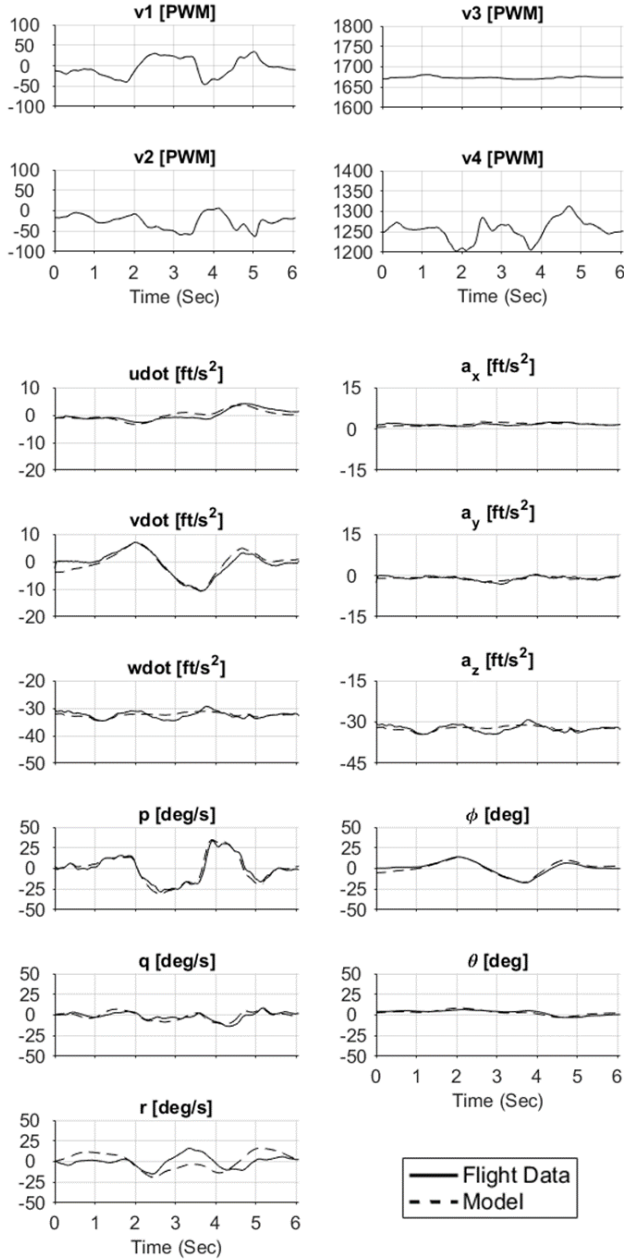


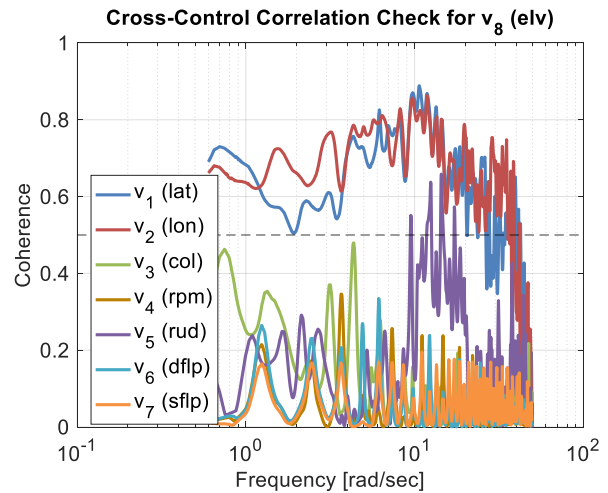
Figure 11. Time-domain verification results for the Scaled Demonstrator at hover.

Table 8. Time-Domain Costs at Hover

Doublet Maneuver	J_{rms}	TIC
Pilot Lat Cyclic (r_1)	3.60	0.24
Pilot Lon Cyclic (r_2)	3.40	0.25
Pilot Collective (r_3)	2.78	0.27
Pilot Pedal (r_4)	3.22	0.22

Frequency-Domain System Identification and Time-Domain Verification at 26 kt

The 26 kt flight condition is the first condition at which the aerosurfaces (rudder, differential flaperon, symmetric flaperon, and elevator) become sufficiently effective for identification, provide control redundancy, and therefore are included in the model structure. As with hover, the JIO Method was required at 26 kt for virtual effectors that had high cross-control correlations. As shown in Figure 12, the elevator virtual effector v_8 had high cross-control correlations with the longitudinal cyclic v_2 and lateral cyclic v_1 virtual effectors. The average cross-control correlations are greater than 0.5 and the secondary control autospectra ($G_{v_2v_2}$, $G_{v_1v_1}$) were within (or close to being within) 20 dB of the primary control autospectrum ($G_{v_8v_8}$). The high cross-control correlations for this virtual effector are due to the redundancy of the v_8 and v_2 virtual effectors, which both primarily affect aircraft pitch motion. The resulting pitch response to elevator v_8 inputs is fed back to longitudinal cyclic v_2 through the control system during closed-loop system identification. As previously discussed for hover, at 26 kt, the large longitudinal cyclic v_2 response in turn results in a relatively large, highly correlated lateral cyclic v_1 response as well due to pitch-roll coupling.



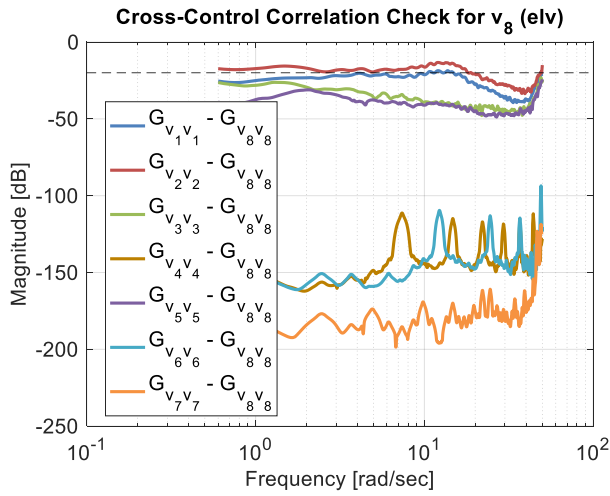


Figure 12. The elevator (v_8) virtual effector has high cross-control correlations with the longitudinal cyclic (v_2) and lateral cyclic (v_1) virtual effectors.

Table 9 lists the frequency response generation methods (Direct and JIO Method cases) used for system identification at 26 kt. Table 10 lists the method used for each frequency response.

Table 9. Freq. Response Generation Methods at 26 kt

Method	Sweep Type	Identified Effector Responses
Direct Method	Ref. input (r) corresponding to effector (v) only	Virtual effector (v) of interest only
JIO Case A	Pilot Lat Cyclic (r_1)	Lat Cyclic (v_1)
	Pilot Lon Cyclic (r_2)	Lon Cyclic (v_2)
	Pilot Collective (r_3)	Collective (v_3)
	Pilot Pedal (r_4)	Rudder (v_5)
JIO Case B	Pilot Lat Cyclic (r_1)	Lat Cyclic (v_1)
	Pilot Lon Cyclic (r_2)	Lon Cyclic (v_2)
	Pilot Pedal (r_4)	Rudder (v_5)
	Diff Flap (r_6)	Diff Flap (v_6)
JIO Case C	Pilot Lat Cyclic (r_1)	Lat Cyclic (v_1)
	Pilot Lon Cyclic (r_2)	Lon Cyclic (v_2)
	Elevator (r_8)	Elevator (v_8)

Table 10. Method Used for Each Freq. Response at 26 kt

Identification Step	Response	Method
Freq. Resp. Included in Step 1	\dot{v}/v_1	JIO Case A
	p/v_1	JIO Case A
	q/v_1	JIO Case A
	r/v_1	JIO Case A
	a_y/v_1	JIO Case A
	\dot{u}/v_2	JIO Case A
	\dot{w}/v_2	JIO Case A
	p/v_2	JIO Case A
Freq. Resp. Added in Step 2	q/v_2	JIO Case A
	a_x/v_2	JIO Case A
	a_z/v_2	JIO Case A
	\dot{u}/v_3	JIO Case A
	\dot{w}/v_3	JIO Case A
	q/v_3	JIO Case A
	a_x/v_3	JIO Case A
	a_z/v_3	JIO Case A
Freq. Resp. Added in Step 2	\dot{u}/v_4	Direct Method
	a_x/v_4	Direct Method
	\dot{v}/v_5	JIO Case A
	r/v_5	JIO Case A
	a_x/v_5	JIO Case A
	\dot{v}/v_6	JIO Case B
	p/v_6	JIO Case B
	r/v_6	JIO Case B
	a_x/v_6	JIO Case B
	\dot{u}/v_7	Direct Method
	\dot{w}/v_7	Direct Method
	a_x/v_7	Direct Method
a_z/v_7	Direct Method	
\dot{w}/v_8	JIO Case C	
q/v_8	JIO Case C	

Figures 13 and 14 show the on-axis frequency responses. As expected, the responses to the aerosurfaces – differential flaperon (v_6), symmetric flaperon (v_7), and elevator (v_8) – which were excited using direct actuator sweeps (as opposed to tracking command sweeps) only have high coherence at high frequency, whereas the coherences for the remaining virtual effectors were high over a wide frequency range. As described earlier in the paper, this is due to the use of direct actuator sweeps, which were required for the aerosurfaces, resulting in lower signal-to-noise ratio and coherence.

A method for combining multiple Direct and JIO Method cases was used for the Bell V-280 [13] to leverage the best quality data for state-space identification; an enhancement of this method using a two-step approach was developed, used, and discussed thoroughly herein. Figure 15 shows the derivatives included in the model structure and Table 10 shows the corresponding frequency responses used during each step of the identification.

In the first step, only the stability derivatives (low frequency) and rotor, VTDP RPM, and rudder control derivatives and time delays (high frequency) were included in the model structure and identified using the rotor, VTDP RPM, and rudder frequency responses only. In the second step, the parameters identified in the first step were frozen and only the remaining aerosurface control derivatives and time delays (high frequency) were identified using all of the frequency responses. This method ensured that the highest quality data were used to determine the core set of parameters in the model, which was then augmented to include the aerosurface parameters. The resulting model has an average frequency-domain cost $J_{ave} = 67$, which meets the $J_{ave} < 100$ guideline and indicates good agreement between the model and flight data. Additionally, as shown in Figure 14, while only a small

frequency range was used for the second identification step, the model actually compares well over a wide frequency range (due to the fact that the low-frequency dynamics are frozen from the first step). A similar system identification approach was used at 39 kt.

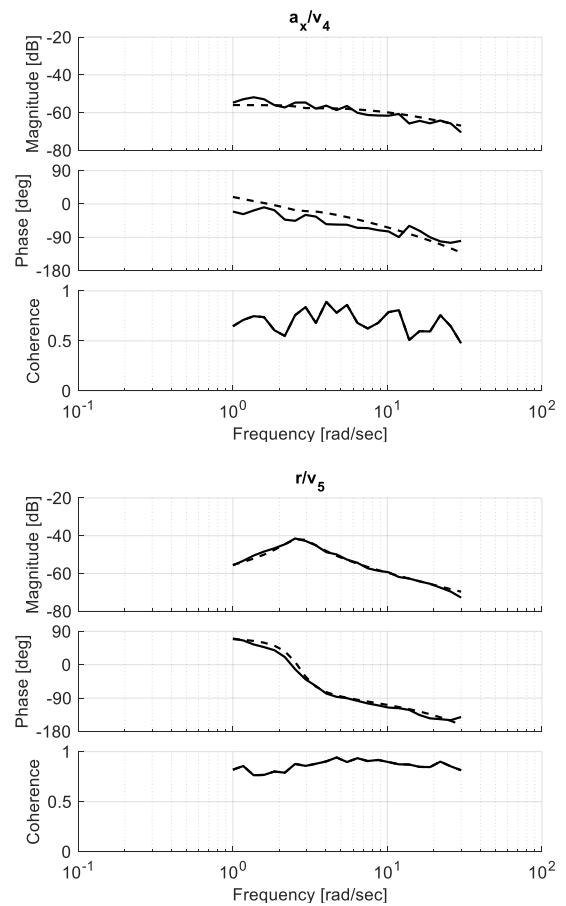
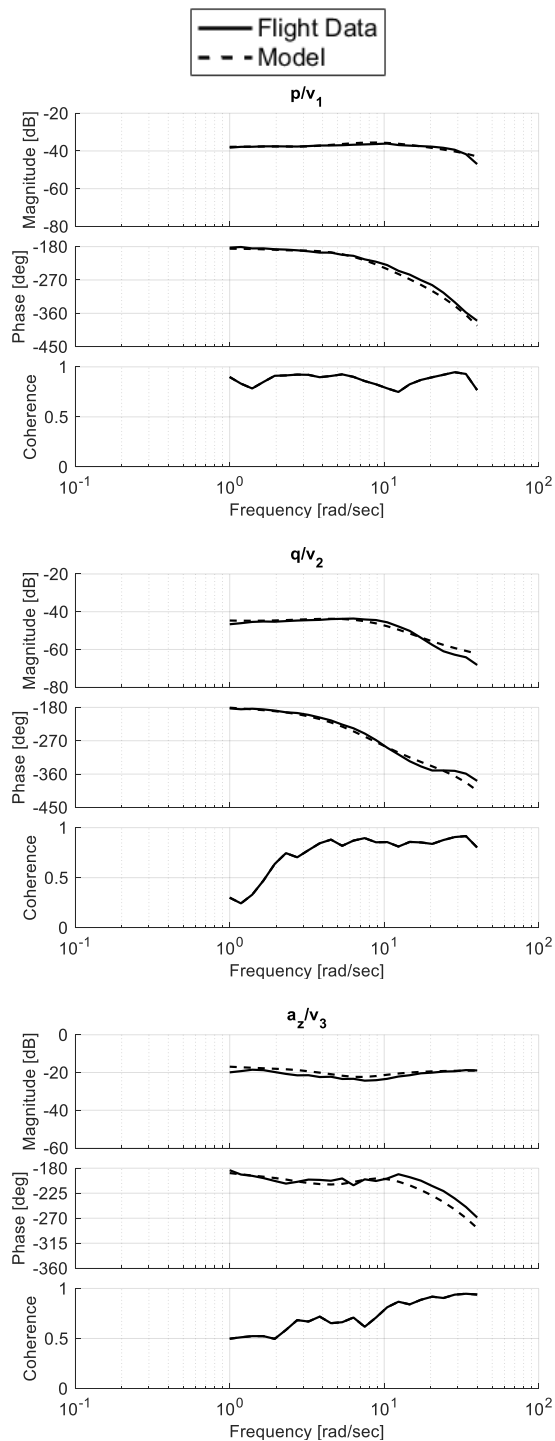
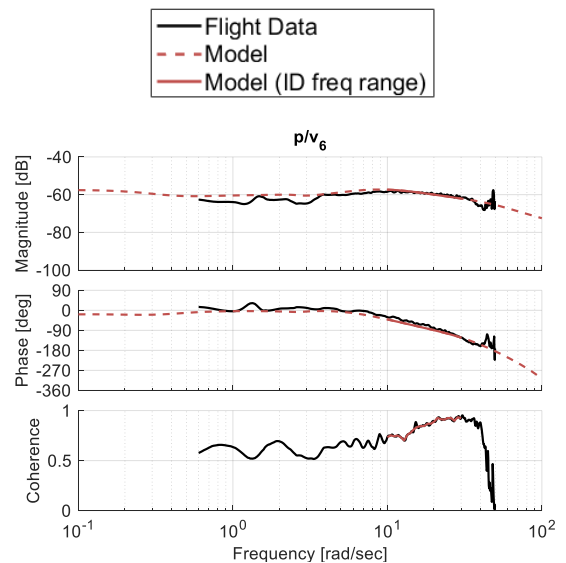


Figure 13. On-axis frequency responses for the first identification step (low and high frequency) at 26 kt.



parameters as indicated by their low insensitivity ($I < 10\%$) and Cramér-Rao bound ($CR < 20\%$) values.

Table 11. Frequency Response Costs at 26 kt

Response	Cost	Freq. [rad/s]
\dot{v}/v_1	23.1	1.0-35
p/v_1	32.1	1.0-40
q/v_1	45.0	2.0-25
r/v_1	89.5	1.0-35
a_y/v_1	77.6	2.0-30
\dot{u}/v_2	114.8	1.0-40
\dot{w}/v_2	49.1	1.0-40
p/v_2	139.4	2.0-30
q/v_2	90.5	1.0-40
a_x/v_2	113.0	3.0-40
a_z/v_2	88.5	1.0-40
\dot{u}/v_3	43.3	1.0-40
\dot{w}/v_3	76.0	2.0-40
q/v_3	205.1	1.0-40
a_x/v_3	94.7	3.0-30
a_z/v_3	70.7	1.0-40
\dot{u}/v_4	43.1	2.0-30
a_x/v_4	168.7	1.0-30
\dot{v}/v_5	34.3	1.0-30
r/v_5	37.5	1.0-30
a_y/v_5	21.0	1.0-30
\dot{v}/v_6	10.7	10-30
p/v_6	42.5	10-30
r/v_6	95.4	10-30
a_y/v_6	13.1	10-30
\dot{u}/v_7	28.1	8.0-35
\dot{w}/v_7	50.0	20-40
a_x/v_7	28.9	8.0-35
a_z/v_7	61.5	15-40
\dot{w}/v_8	24.6	8.0-35
q/v_8	54.1	8.0-35
I_{ave}	66.6	-

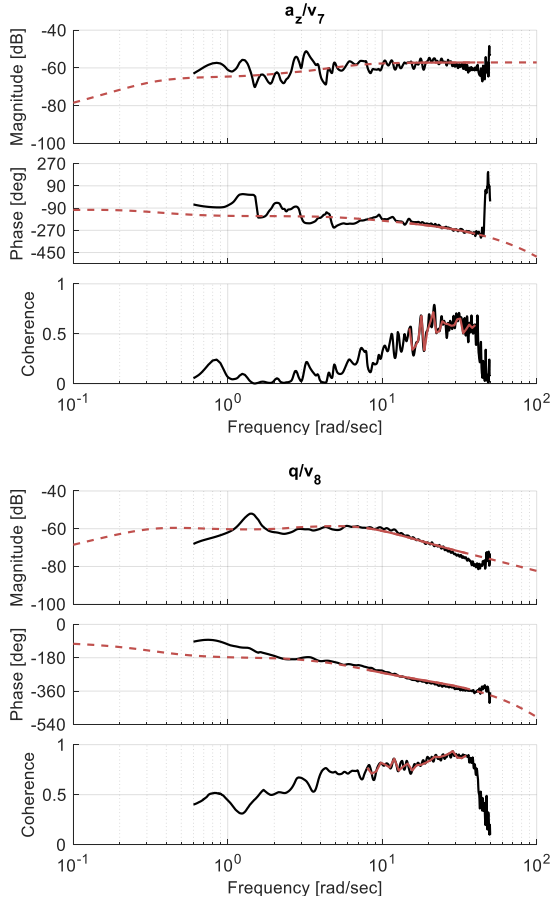


Figure 14. On-axis frequency responses for the second identification step (high frequency only) at 26 kt.

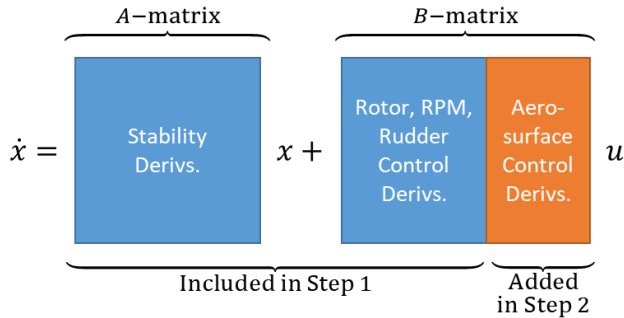


Figure 15. Derivatives included during each step of the identification.

Table 11 shows costs associated with each frequency response at 26 kt. Overall, on-axis frequency response mismatch costs, as well as the average mismatch cost, are low indicating good model accuracy. Almost all of the off-axis responses are within the guideline for individual frequency response costs of 150-200 [6]. Slightly higher costs are typical for the off-axis responses since they have lower excitation, and therefore lower coherence, than the on-axis responses during frequency sweeps. Table 12 shows the identified parameters and the associated Cramér-Rao bounds (CR) and insensitivities (I) at 26 kt [6]. All identified parameters are known to good accuracy and not correlated with any other

Table 12. Parameters Identified at 26 kt

Parameter	Value	CR (%)	I (%)
τ_f	0.028614	3.0	0.5
X_u	-0.52144	11.3	5.2
X_w	0 ^b	-	-
X_q	0 ^b	-	-
X_r	0 ^b	-	-
$X_{\beta_{1c}}$	26.5236	3.8	0.9
X_η	0.0015246	3.3	1.6
Y_v	-0.22062	5.6	2.5
Y_p	0.17785 ^c	-	-
Y_r	-0.18118 ^c	-	-
$Y_{\beta_{1s}}$	$-X_{\beta_{1c}}$ ^a	-	-
Y_η	-0.00084614 ^c	-	-
Z_u	0 ^b	-	-

Parameter	Value	CR (%)	I (%)
Z_w	-3.0842	5.7	2.2
Z_q	0 ^b	-	-
L_u	0 ^b	-	-
L_v	0.24334 ^c	-	-
L_w	-1.0253 ^c	-	-
$L\beta_{1s}$	-867.38 ^c	-	-
M_u	0.099043 ^c	-	-
M_v	0 ^b	-	-
M_w	-0.56921	13.1	4.7
$M\beta_{1c}$	-199.8349	4.1	0.8
N_v	0.54568	2.1	0.9
N_w	-0.2101	25.2	8.9
N_p	-1.2929	4.4	1.0
N_r	-0.92996	6.8	2.9
N_η	0.0067278 ^c	-	-
$Mf\beta_{1s}$	-0.57536	8.2	2.6
$Lf\beta_{1c}$	0.92931	4.7	1.5
ω_c	-9.684 ^c	-	-
X_{v_3}	0.004529	9.6	4.3
X_{v_7}	-0.0011237	2.7	1.3
X_{v_8}	0 ^b	-	-
Y_{v_5}	-0.001799	7.0	3.4
Y_{v_6}	0 ^b	-	-
Z_{v_2}	0.013974	5.1	2.1
Z_{v_3}	-0.11368	3.3	1.6
Z_{v_7}	-0.0013982	3.8	1.9
Z_{v_8}	0 ^b	-	-
L_{v_3}	0 ^b	-	-
L_{v_5}	0 ^b	-	-
L_{v_6}	0.021876	2.6	1.1
M_{v_3}	0.060075	4.0	1.5
M_{v_7}	0 ^b	-	-
M_{v_8}	-0.007473	3.0	1.5
N_{v_1}	-0.019577	4.4	1.0
N_{v_3}	-0.012123 ^c	-	-
N_{v_5}	0.0097714	3.0	1.3
N_{v_6}	0 ^b	-	-
Mf_{v_1}	0.00013949	7.4	2.5
Mf_{v_2}	0.00020999	4.0	0.9
Lf_{v_1}	0.00035633 ^c	-	-
Lf_{v_2}	-7.9709e-05 ^c	-	-
τ_{v_1}	0.045011	3.9	1.8
τ_{v_2}	0.044248	3.0	1.4
τ_{v_3}	0.048890	2.8	1.4
τ_{v_4}	0.034927	9.5	4.7
τ_{v_5}	0.043252	5.8	2.8
τ_{v_6}	0.038098	4.1	1.6
τ_{v_7}	0.053319	2.0	1.0
τ_{v_8}	0.040158	4.2	2.1

^a Constrained parameter

^b Eliminated parameter from model structure

^c Fixed parameter in model

Figure 16 shows time-domain verification results for a piloted lateral doublet at 26 kt. As shown in Table 13, the results meet the $J_{rms,Fr} < 6.2$ and $TIC < 0.3$ guidelines previously discussed indicating good agreement between the model and flight data.

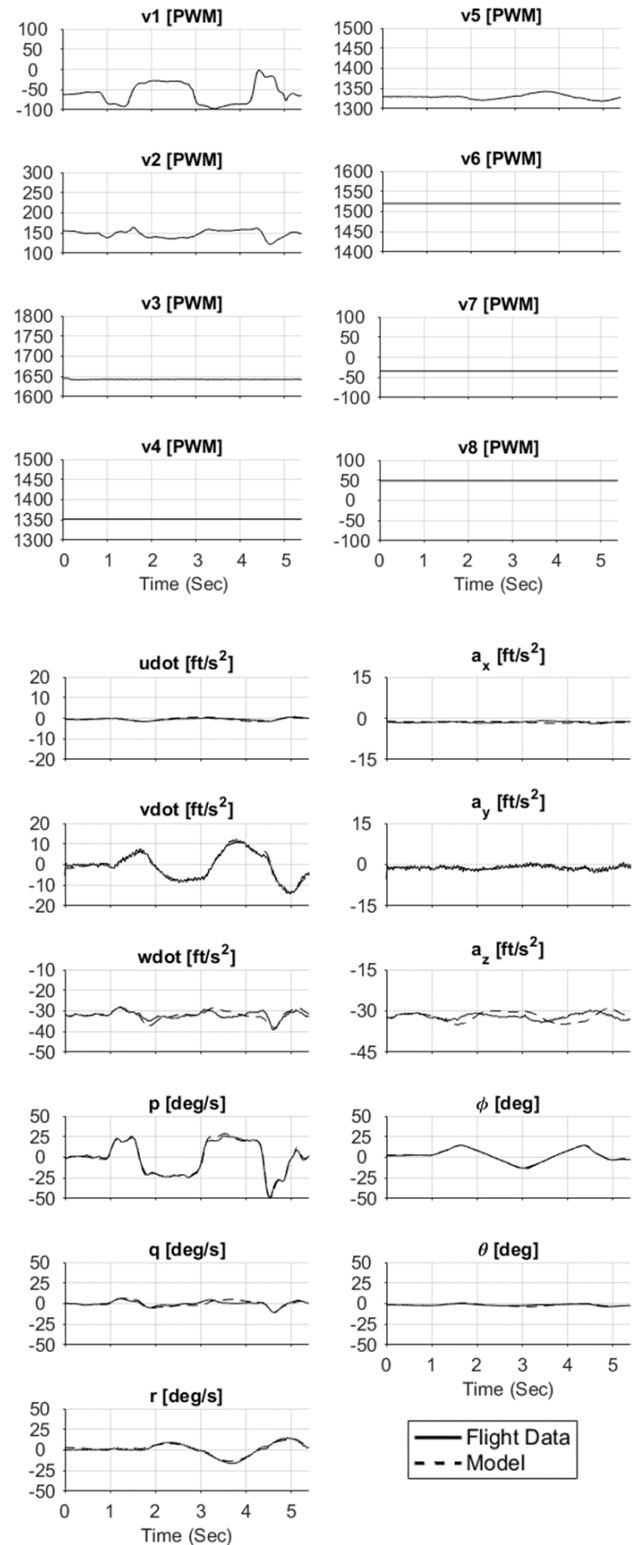


Figure 16. Time-domain verification results for the Scaled Demonstrator at 26 kt.

Table 13. Time-Domain Costs at 26 kt

Doublet Maneuver	J_{rms}	TIC
Pilot Lat Cyclic (r_1)	1.24	0.08
Pilot Lon Cyclic (r_2)	2.06	0.14
Pilot Collective (r_3)	2.74	0.20
Pilot Pedal (r_4)	2.61	0.16

ADDITIONAL DISCUSSION OF IDENTIFICATION METHODS AND RESULTS

This section covers a few points of discussion for system identification that are not covered elsewhere in the paper. This includes (1) selection of frequency responses when both the Direct and JIO Methods are available, (2) comparison of the Scaled Demonstrator's lateral rotor flap stiffness with those of other small-scale helicopters, and (3) challenges that were encountered for system identification at 13 kt.

Frequency Response Selection When Both the Direct Method and JIO Method Are Available

In this study, there were a few cases where a given frequency response was available from both the Direct and JIO Methods. Prior work on the Bell V-280 also compared the Direct and JIO Methods [13, 14] and it was found that Direct Method may produce satisfactory accuracy and better quality and should be used. In this study, a similar approach is used, expanded upon, and discussed thoroughly.

The yaw rate frequency responses to collective (r/v_3) and VTDP RPM (r/v_4), respectively, at hover provide a good example of how to decide whether to use the Direct or JIO Method. As shown in Table 4, JIO Case B can be used to obtain both the r/v_3 and r/v_4 frequency responses. However, as will be discussed in this section, the JIO Method is only required for the r/v_3 response (due to high cross-control correlation), whereas an accurate result for r/v_4 can be obtained using the Direct Method.

Figure 17 shows the cross-control correlation check for the collective v_3 virtual effector at hover. It indicates that collective v_3 control inputs are highly correlated with VTDP RPM v_4 control inputs since the average cross-control coherence for v_3 with v_4 is greater than 0.5 and the secondary control autospectrum ($G_{v_4 v_4}$) is large relative to the primary control autospectrum ($G_{v_3 v_3}$). Thus, the JIO Method is required to obtain frequency responses to v_4 accurately. The high correlation results from collective-yaw coupling, which is typical for helicopters at hover. The collective input produces an increase in torque from the rotor on the fuselage, which produces a yaw response. The yaw response is fed back through the control system and in turn produces a response by the VTDP RPM, which provides yaw control at hover.

Figure 18 shows the cross-control correlation check for the VTDP RPM v_4 virtual effector at hover. Conversely, it indicates that the VTDP RPM v_4 has very low correlation with

collective v_3 since the average cross-control coherence is well below 0.5. Therefore, the Direct Method will provide an accurate frequency response. Together, the results of the cross-control correlation checks in Figures 17 and 18 indicate that the coupling is one-way: collective control inputs result in a correlated VTDP RPM response, but VTDP RPM inputs *do not* result in a correlated collective response.

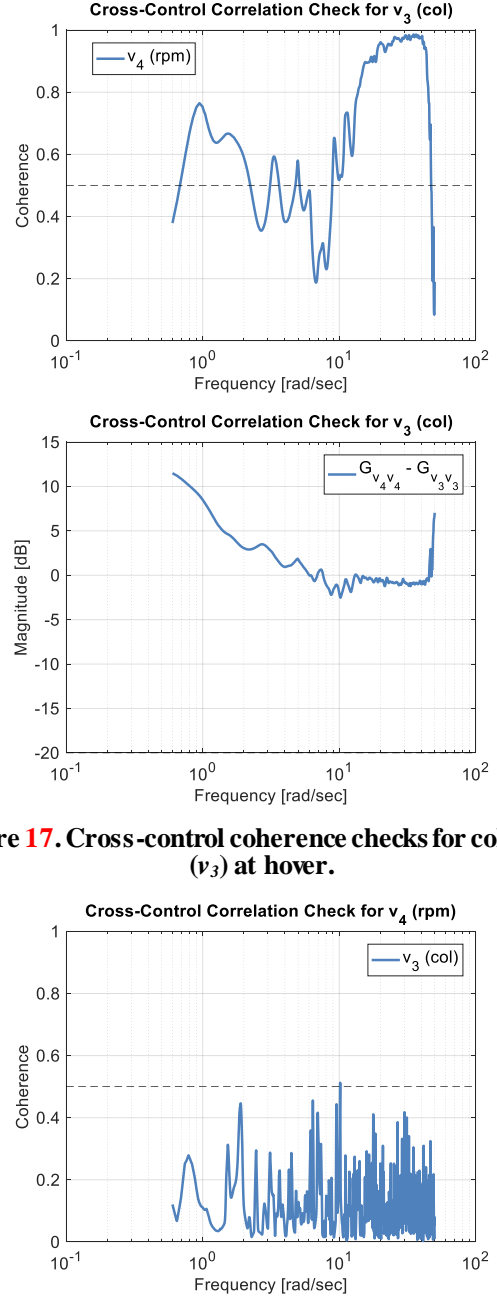


Figure 17. Cross-control coherence checks for collective (v_3) at hover.

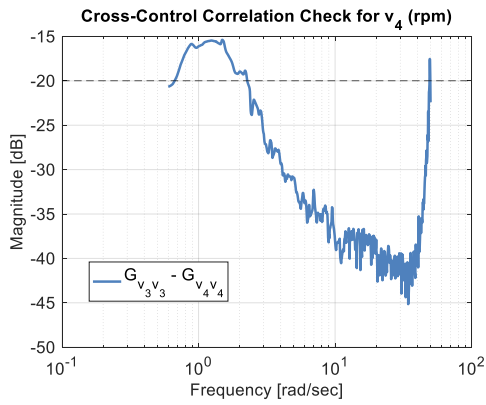


Figure 18. Cross-control coherence checks for the VTDP RPM (v_4) at hover.

Figures 19 and 20 compare the Direct and JIO Methods for the yaw rate frequency responses to collective (r/v_3) and VTDP RPM (r/v_4), respectively. For the r/v_3 frequency response, there is a large difference between the two methods since the JIO Method correctly accounts for the effect of the highly correlated controls, whereas the Direct Method does not. Conversely, for the r/v_4 frequency response, the results for the two methods are very similar since the cross-control correlations are low and the Direct Method gives an accurate result (with higher coherence than the JIO Method). This result corroborates those of the V-280 work [13, 14] where the Direct Method results sometimes can and should be used in place of the JIO Method. Thus, as shown in Table 5, the JIO Method frequency response was used for system identification for r/v_3 , whereas the Direct Method was used for r/v_4 . Figure 21 shows the time-domain verification of the yaw rate response during a pilot collective doublet, which confirms the accuracy of the JIO Method used for r/v_3 .

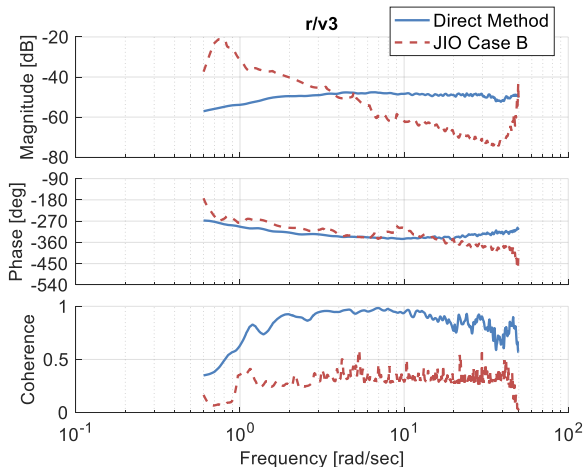


Figure 19. The JIO Method is required since the cross-control correlations for v_3 are high.

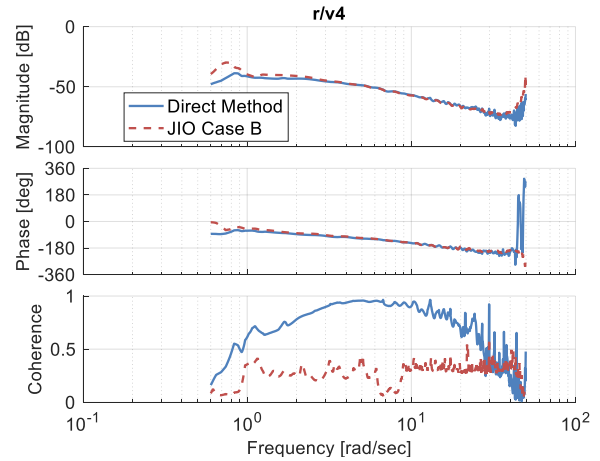


Figure 20. The Direct Method provides accurate results since the cross-control correlations for v_4 are low.

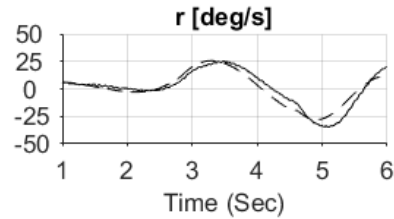


Figure 21. Time-domain verification of yaw rate response during pilot collective doublet confirms accuracy of the JIO Method used for r/v_3 .

Note that the JIO Method would typically also be required to accurately obtain the hover \dot{w}/v_3 and a_z/v_3 frequency responses shown in Figure 22, as there was high cross-control correlation with v_4 during the v_3 sweep. However, this is a special case where the Direct Method also provides accurate results since the heave dynamics are largely decoupled in hover (i.e. no dynamic or control coupling from yaw to heave), and therefore are not affected by feedback in the yaw axis. This is confirmed by the frequency responses in Figure 22, which are nearly identical between the two methods, as well as by the \dot{w} equation of motion (Equation 8) since there is no Z_r stability derivative or Z_{v_4} control derivative (i.e. the yaw response and control input do not have any effect on the vertical response). Therefore, as shown in Table 5, the Direct Method was used for \dot{w}/v_3 and a_z/v_3 since it has higher coherence than the JIO Method.

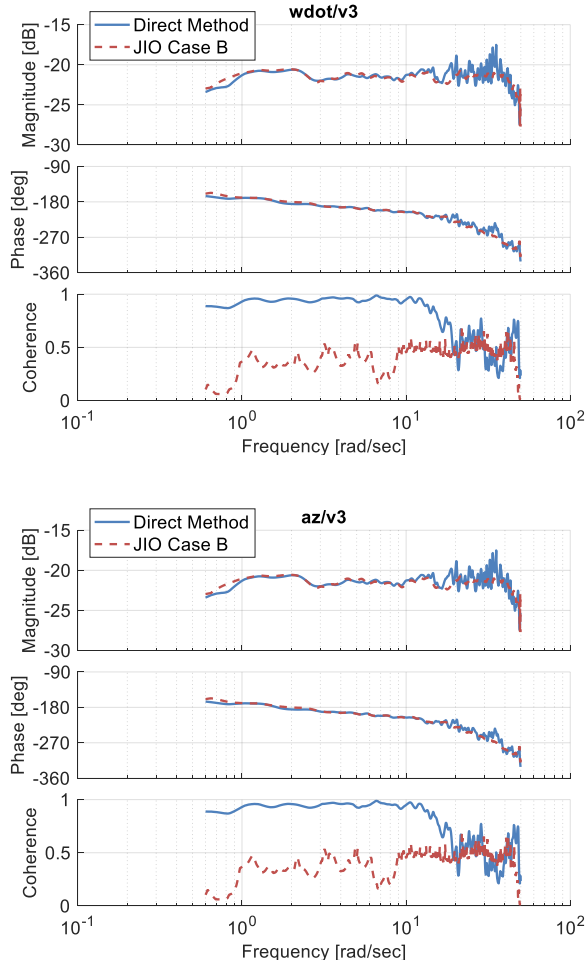


Figure 22. This is a special case where the Direct Method is accurate since there is no dynamic or control coupling from yaw to collective.

Lateral Rotor Flap Stiffness Comparison at Hover

Table 14 compares the lateral rotor flap stiffness of the Scaled Demonstrator with those of other smaller-scale helicopters. The Scaled Demonstrator has a flybarless main rotor and is used as the reference scale (i.e. $\ell = 1$). Since the units of rotor flap stiffness are s^{-2} , the values scale directly with N [6]. Normalizing for scale, the table shows that the ADAPT Scaled Demonstrator has the third highest rotor flap stiffness behind the Yamaha R-MAX [15], which has a very high stiffness resulting from its teetering rotor head (no flapping hinges) with hard elastomeric restraint, and the 360CFX [16], another flybarless helicopter. The Raptor [17] and small-scale Honeybee [6] have lower normalized stiffness values.

Table 14. Rotor Flap Stiffness

Vehicle	Rotor D [ft]	ℓ	$ L_{\beta_{1s}} $ (scaled)
R-MAX	10.25	0.5	588.9 (1081.8)
ADAPT TM SD	5.58	1.0	785.2
Raptor 50	4.41	1.3	735.5 (581.3)
360CFX	2.67	2.1	5115.2 (2447.6)
Honeybee	1.66	3.4	1273.0 (378.7)

Challenges for System Identification at 13 kt

Identifying frequency responses with sufficient coherence at 13 kt was particularly challenging due to the highly coupled dynamics, lack of yaw authority, and reduced controllability of the Scaled Demonstrator at this flight condition. As previously noted, the VTDP sector is fully deflected in hover to direct airflow to provide anti-torque and yaw control, and fully retracted at 26 and 39 kt to provide forward thrust, with rudder providing yaw control. However, at 13 kt, the rudder is not yet effective for yaw control and the VTDP sector is only partially rotated, resulting in VTDP RPM control producing both yaw rate r and longitudinal speed u . The introduction of yaw and longitudinal motion simultaneously is problematic due to the highly coupled nature of the aircraft, which relies on the control system to decouple the responses. Additionally, the split VTDP RPM control effectiveness between yaw and forward thrust results in limited yaw authority. The test pilot confirmed that these factors resulted in reduced controllability of the aircraft at 13 kt making it difficult to maintain trim. As exemplified by Figure 23, the resulting frequency responses obtained at this flight condition were generally of poorer quality than the other flight conditions (i.e. lower signal-to-noise ratio and coherence), particularly for the yaw axis. Despite this, it was still possible to identify a state-space model at 13 kt with cost $J_{ave} < 100$, indicating good agreement between the model and flight data.

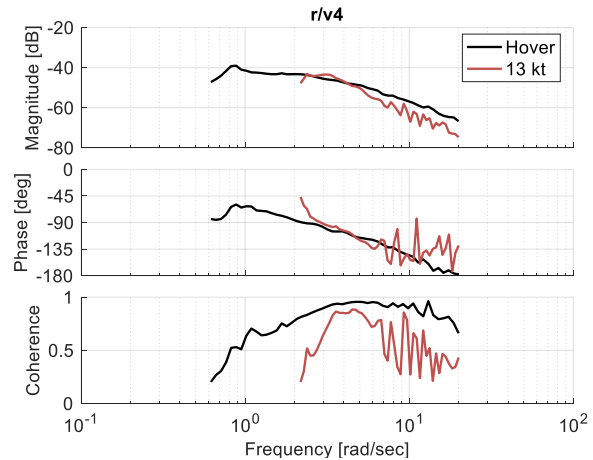


Figure 23. Data quality at 13 kt was significantly poorer than other flight conditions as exemplified by the r/v_4 response at 13 kt relative to hover.

STITCHED MODEL RESULTS

The STITCH software tool [3] was used to generate a continuous full-envelope stitched model from the point identification models and trim data at hover, 13, 26, and 39 kt. The stitched model is a time-varying, quasi-nonlinear model where the stability and control derivatives are stored in lookup tables and combined with the full nonlinear equations of motion and gravitational force equations. This modeling technique is in the class of quasi-linear-parameter-varying (qLPV) models with total x-axis body velocity U as the stitching parameter [18, 19].

Trim Data Trends with Airspeed

Figure 24 shows the trim data, which were obtained from the point models for use in the stitched model, versus airspeed. STITCH uses a cubic spline (not shown) to interpolate intermediate trim points for continuity in the stitched model. Note that finely spaced trim-shot data [3] was not available for this study, but can be used in general to improve the accuracy of trim data at airspeeds between the point model airspeeds.

Pitch attitude trim θ_0 decreases (becomes more nose down) to tilt the rotor disc forward as necessary to provide forward thrust with increasing airspeed. As previously noted, the z-body axis velocity trim was approximated as $W_0 = V_T \sin \alpha_0$, where $\alpha_0 = \theta_0$ in trim (i.e. level flight). Increasingly negative z-body axis velocity trim W_0 indicates that upward body-axis velocity is required to maintain level flight for the given trim pitch attitude θ_0 .

Trim states $\beta_{1c,0}$ and $\beta_{1s,0}$ were not measured and were instead estimated by calculating the trim gradients required to match the u -derivatives of the linearized stitched model to those of the point identification models. For brevity, this process is demonstrated here using a subset of the u -derivatives (X_u , Y_u , L_u , and M_u) at the hover and 13 kt models only.

In trim, the left-hand side of each equation of motion corresponding to these four derivatives (\dot{u} , \dot{v} , \dot{p} , and \dot{q}) is zero. Solving each equation for the corresponding u -derivative gives X_u , Y_u , L_u , and M_u in terms of derivatives and trim gradients with respect to u . For example, for the \dot{u} equation:

$$X_{u_{\text{stitch}}} = -X_w \frac{\Delta w}{\Delta u} + (g \cos \theta_0) \frac{\Delta \theta}{\Delta u} - X_{\beta_{1c}} \frac{\Delta \beta_{1c}}{\Delta u} - X_\eta \frac{\Delta \eta}{\Delta u} - X_{v_3} \frac{\Delta v_3}{\Delta u} - X_{v_7} \frac{\Delta v_7}{\Delta u} - X_{v_8} \frac{\Delta v_8}{\Delta u}$$

Equation 15

Since all trim gradients are known except for those of the flapping states, $\Delta \beta_{1c}/\Delta u$ and $\Delta \beta_{1s}/\Delta u$ can be solved to match the stitched model u -derivatives to those of the point identification models:

$$\begin{aligned} X_{u_{\text{ID}}} - X_{u_{\text{stitch}}} &= \Delta X_u = -X_{\beta_{1c}} \frac{\Delta \beta_{1c}}{\Delta u} \\ M_{u_{\text{ID}}} - M_{u_{\text{stitch}}} &= \Delta M_u = -M_{\beta_{1c}} \frac{\Delta \beta_{1c}}{\Delta u} \\ Y_{u_{\text{ID}}} - Y_{u_{\text{stitch}}} &= \Delta Y_u = -Y_{\beta_{1s}} \frac{\Delta \beta_{1s}}{\Delta u} \\ L_{u_{\text{ID}}} - L_{u_{\text{stitch}}} &= \Delta L_u = -L_{\beta_{1s}} \frac{\Delta \beta_{1s}}{\Delta u} \end{aligned} \quad \text{Equation 16}$$

Putting these equations in matrix form and including terms for two consecutive flight conditions (hover and 13 kt) gives:

$$\begin{bmatrix} -X_{\beta_{1c}|_0} & 0 & 0 & 0 \\ 0 & -X_{\beta_{1c}|_{13}} & 0 & 0 \\ 0 & 0 & -Y_{\beta_{1s}|_0} & 0 \\ 0 & 0 & 0 & -Y_{\beta_{1s}|_{13}} \\ -M_{\beta_{1c}|_0} & 0 & 0 & 0 \\ 0 & -M_{\beta_{1c}|_{13}} & 0 & 0 \\ 0 & 0 & -L_{\beta_{1s}|_0} & 0 \\ 0 & 0 & 0 & -L_{\beta_{1s}|_{13}} \end{bmatrix} \begin{bmatrix} \frac{\Delta \beta_{1c}}{\Delta u}|_0 \\ \frac{\Delta \beta_{1c}}{\Delta u}|_{13} \\ \frac{\Delta \beta_{1s}}{\Delta u}|_0 \\ \frac{\Delta \beta_{1s}}{\Delta u}|_{13} \end{bmatrix} = \begin{bmatrix} \Delta X_u|_0 \\ \Delta X_u|_{13} \\ \Delta Y_u|_0 \\ \Delta Y_u|_{13} \\ \Delta L_u|_0 \\ \Delta L_u|_{13} \\ \Delta M_u|_0 \\ \Delta M_u|_{13} \end{bmatrix}$$

Equation 17

This system of equations can be solved to obtain the β_{1c} and β_{1s} trim gradients at each flight condition. However, the trim gradients can be defined explicitly in terms of the trim states using a forward difference method as:

$$\begin{bmatrix} \frac{\Delta \beta_{1c}}{\Delta u}|_0 \\ \frac{\Delta \beta_{1c}}{\Delta u}|_{13} \\ \frac{\Delta \beta_{1s}}{\Delta u}|_0 \\ \frac{\Delta \beta_{1s}}{\Delta u}|_{13} \end{bmatrix} = \begin{bmatrix} -1 & 1 & 0 & 0 & 0 & 0 \\ u_{13} - u|_0 & u_{13} - u|_0 & 0 & 0 & 0 & 0 \\ 0 & -1 & 1 & 0 & 0 & 0 \\ u_{26} - u|_{13} & u_{26} - u|_{13} & 0 & 0 & 0 & 0 \\ 0 & 0 & 0 & -1 & 1 & 0 \\ u_{13} - u|_0 & u_{13} - u|_0 & 0 & 0 & 0 & 0 \\ 0 & 0 & 0 & 0 & -1 & 1 \\ u_{26} - u|_{13} & u_{26} - u|_{13} & 0 & 0 & 0 & 0 \end{bmatrix} \begin{bmatrix} \beta_{1c}|_0 \\ \beta_{1c}|_{13} \\ \beta_{1c}|_{26} \\ \beta_{1s}|_0 \\ \beta_{1s}|_{13} \\ \beta_{1s}|_{26} \end{bmatrix}$$

Equation 18

Equation 18 can be substituted into Equation 17, which can then be solved to directly obtain the trim flapping states $\beta_{1c,0}$ and $\beta_{1s,0}$ at each airspeed. The full calculation of $\beta_{1c,0}$ and $\beta_{1s,0}$ included terms for all the u -derivatives and all flight conditions in the equations.

Note that Equation 17 is an over-constrained problem (i.e., more equations than unknowns), and so the pseudo-inverse solution gives the linear least-squares approximation that best matches the identified u -derivatives. Also note that because Equation 18 is formulated with a difference scheme, it is rank deficient and an infinite number of solutions exist. Physically, this means the trim values can be shifted by a constant without changing their gradient. Herein, the solution is shifted such that the hover flapping states $\beta_{1c,0}$ and $\beta_{1s,0}$ are zero, since it is expected that flapping should be small when the main rotor is producing all of the lift and the roll moment generated by VTDP RPM is negligible ($L_{v_4} = 0$ at hover).

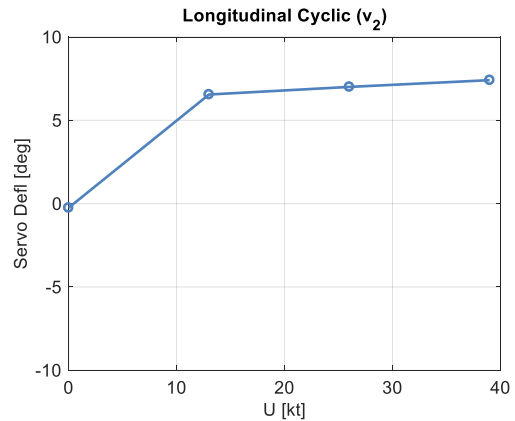
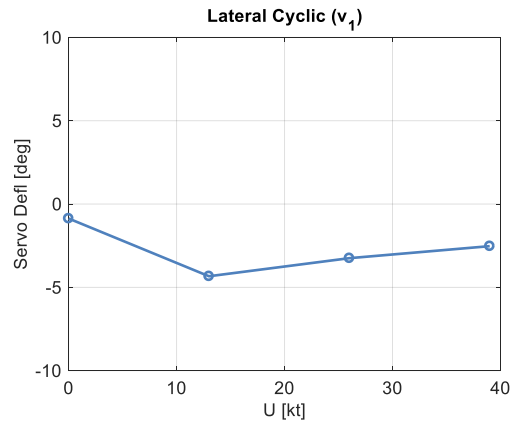
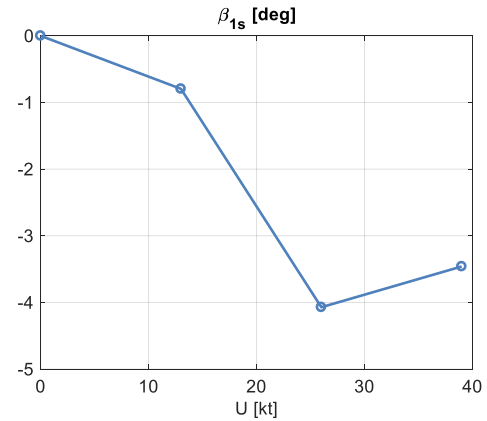
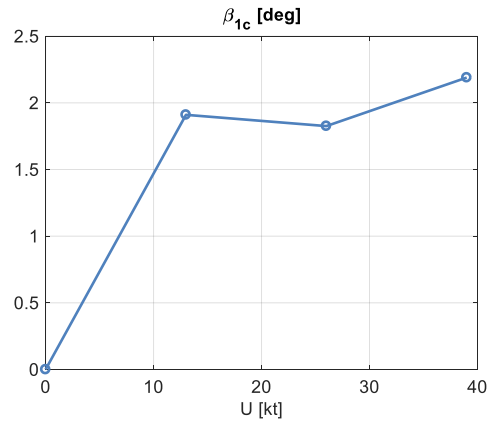
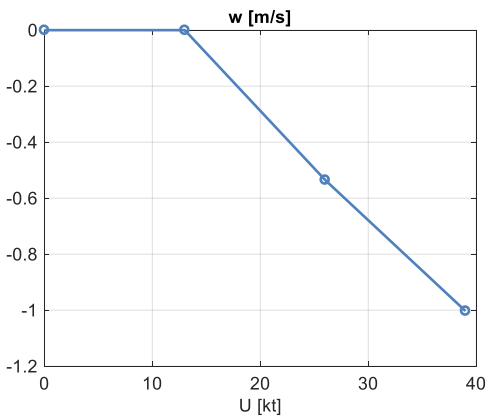
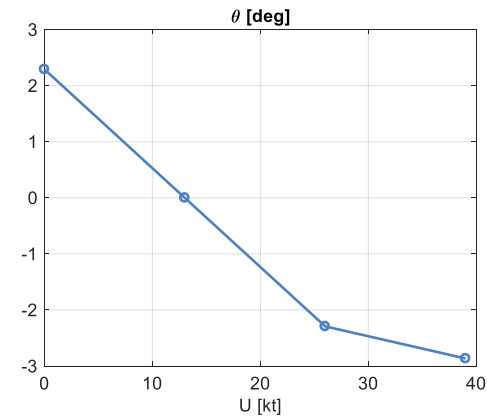
Figure 25 shows an example of one of the u -derivatives as a function of airspeed for the identified models, the stitched model before determining flapping state trim data, and the stitched model with the updated flapping state trim data. The updated flapping state trim data improves the match of the derivative to the identified value.

The results of the $\beta_{1c,0}$ and $\beta_{1s,0}$ calculations are shown in Figure 24. Positive $\beta_{1c,0}$ indicates that the rotor disc is tilted

forward with respect to the x-body axis to provide forward thrust; $\beta_{1s,0}$ transitions from a small positive to negative value (i.e. the rotor disc tilts to the right).

Right lateral cyclic trim $v_{1,0}$ is used to eliminate the side-force resulting from VTDP RPM analogous to conventional helicopters with tail rotors at low speed [20]. Longitudinal cyclic trim $v_{2,0}$ is increased with airspeed to tilt the rotor disc forward and provide forward thrust. Collective trim $v_{3,0}$ follows a trend similar to conventional helicopters where it is at a maximum value at hover, decreases to a minimum value at the minimum drag speed, and then increases again to provide forward thrust at high speed [20, 21, 22]. Because of the rotation of the VTDP sector as airspeed increases, VTDP RPM trim $v_{4,0}$ is adjusted to provide anti-torque at hover and 13 kt and forward thrust at 26 and 39 kt.

As previously discussed, the aerosurfaces are only effective at 26 and 39 kt, where airspeed is high enough for the lift forces on the aerosurfaces to affect aircraft motion. The rudder trim $v_{5,0}$ is rotated with the VTDP sector and provides yaw control at 26 and 39 kt. Differential flaperon $v_{6,0}$ is held at zero such that no roll moment is provided by this effector in trim. At low speed, symmetric flaperon trim $v_{7,0}$ is deflected down to reduce interference with the rotor inflow. At high speed, symmetric flaperon is deflected upwards to oppose nose down pitching moments. Elevator trim $v_{8,0}$ is held at zero across all airspeeds.



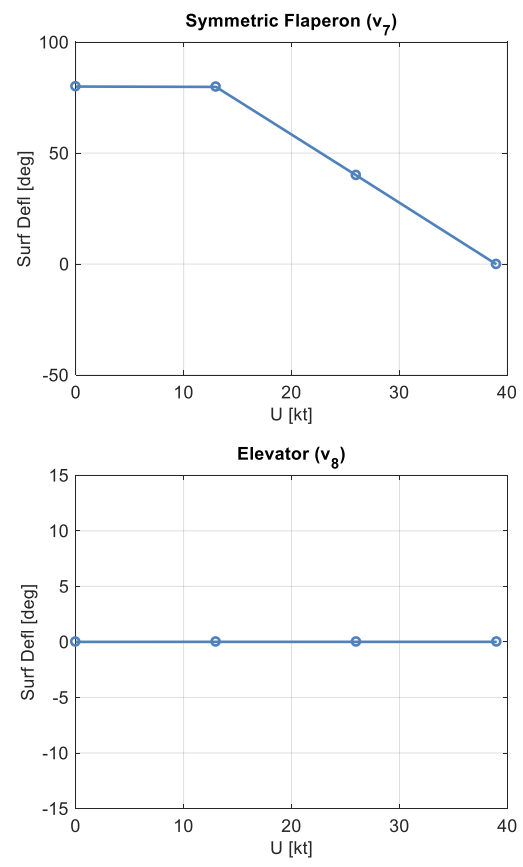
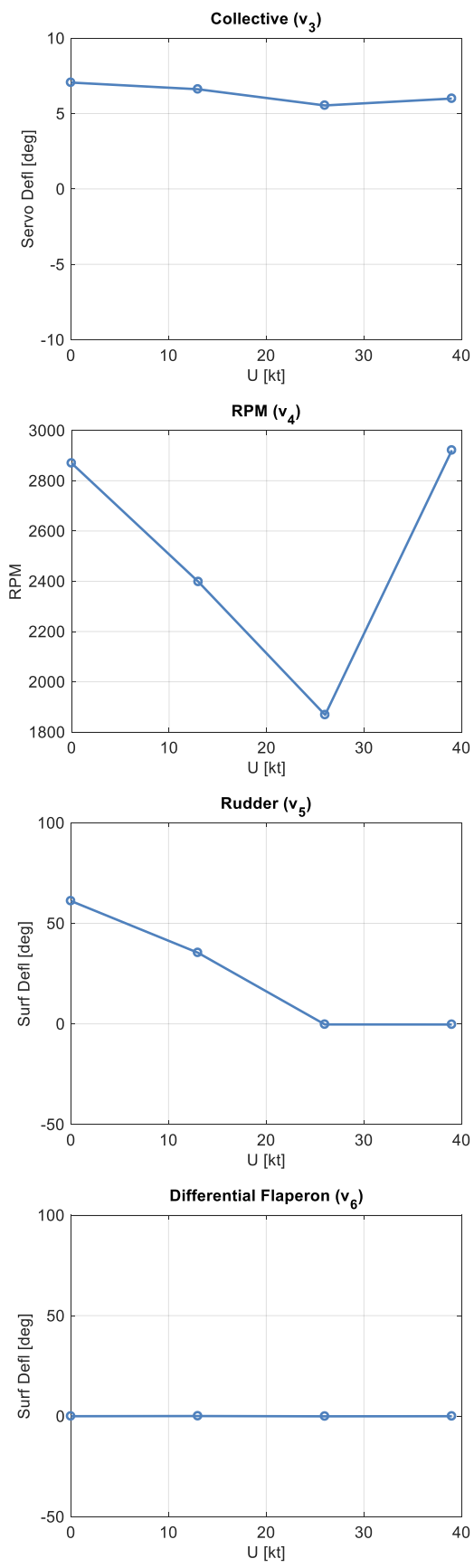


Figure 24. Trim data versus airspeed.

Figure 25. Speed-stability derivative M_u vs. airspeed.

Stability and Control Derivative Trends with Airspeed

This section discusses the trends of the key stability and control derivatives with airspeed. The location of the derivatives in the equations motion (Equation 8) can be observed to provide an understanding of how the control inputs and states affect the aircraft motion.

Figure 26 shows the key on-axis stability derivatives of the linearized stitched model versus airspeed. Derivatives X_u and Y_v are the longitudinal and lateral speed-damping derivatives, respectively, and are negative for all airspeeds indicating that forces oppose perturbations in u and v . At low speed, these derivatives are primarily due to the rotor disc tilt aft and left following perturbations in u and v , respectively [20]. At higher speed, X_u increases in magnitude linearly, which is typical and reflects the increasing drag on the aircraft. The vertical speed-damping derivative Z_w is negative and analogously indicates restorative (stabilizing) forces for perturbation in w . The vertical aircraft response is largely decoupled at low speed and therefore Z_w is the dominant stability derivative, but at high speed the vertical and pitch responses become more coupled.

Stability derivatives $Lf_{\beta_{1s}}$ and $Mf_{\beta_{1c}}$ are the roll and pitch rotor flap stiffnesses. The increase in magnitude of each derivative reflects the increase of restorative roll and pitch moments with airspeed; similar trends were seen in a study of the SH-2G helicopter in [6]. The magnitude of $Lf_{\beta_{1s}}$ is significantly larger than that of $Mf_{\beta_{1c}}$ due to the smaller moment of inertia of the roll relative to pitch axis [6].

The parameter ω_{lag} is the motor lag break frequency that represents the lag associated with speeding up and slowing down the VTDP propeller. It appears as both a stability and control derivative in Figures 26 and 27, respectively, and is constant with airspeed. It effectively sets the bandwidth of the aircraft response to the VTDP RPM virtual effector and introduces lag at frequencies above this bandwidth.

Figure 27 shows the on-axis control derivatives of the linearized stitched model for each virtual effector versus airspeed. The Lf_{v_1} control derivative increases with airspeed, whereas the Mf_{v_2} control derivative decreases with airspeed. The magnitude of the Z_{v_3} control derivative increases with airspeed and indicates that collective produces larger vertical responses at higher airspeeds. The control derivatives N_{v_5} , L_{v_6} , Z_{v_7} and M_{v_8} indicate the primary axis of response for each aerosurface (rudder, differential flaperon, symmetric flaperon, and elevator, respectively). Note that a vertical response to elevator a_z/v_8 would typically be expected for fixed-wing aircraft, but this frequency response and associated control derivative Z_{v_8} could not be identified with sufficient coherence for the Scaled Demonstrator. The monotonic increase in the magnitudes of the aerosurface control derivatives is expected since they are directly related to the increase in lift generated by the aerosurfaces with airspeed.

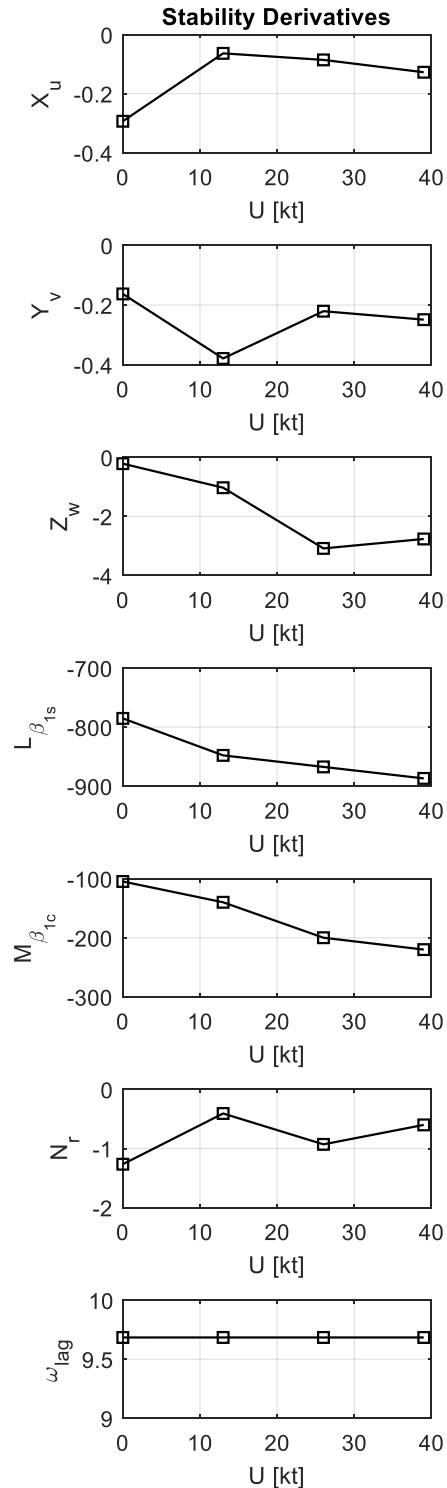


Figure 26. Key on-axis stability derivatives in the linearized stitched model.

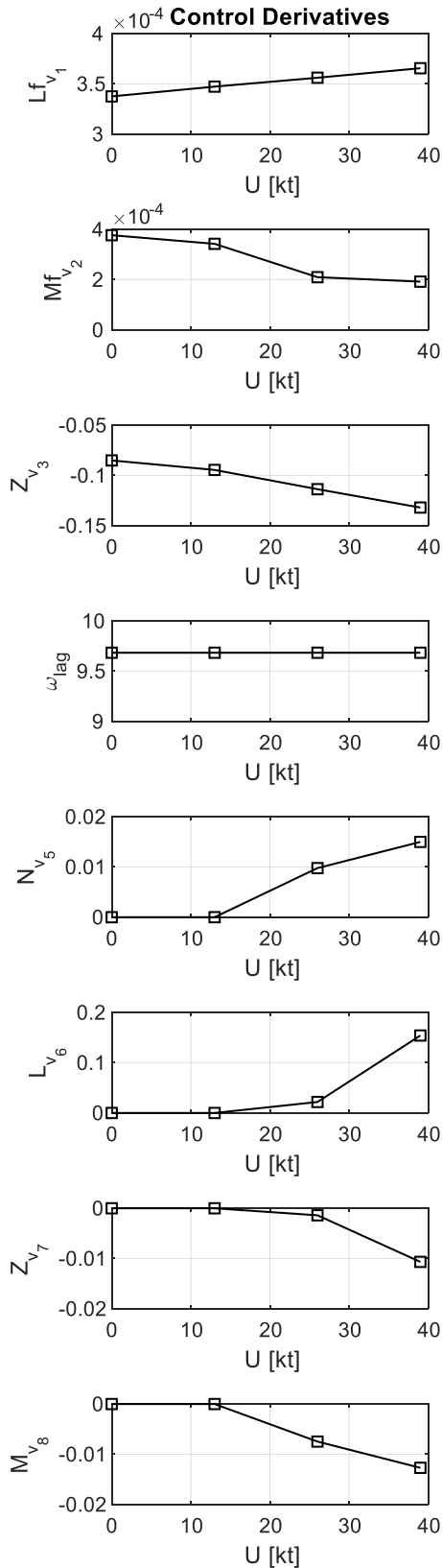


Figure 27. On-axis control derivatives of the linearized stitched model for each virtual effector.

Implications for Control Redundancy

Table 15 summarizes the primary axis of response for each virtual effector for the Scaled Demonstrator. The table shows that control redundancy exists for roll, pitch, and vertical responses at 26 and 39 kt. This is a key result that shows the axes and airspeeds where damage tolerant control (DTC), which relies on control redundancy, will be effective. As discussed earlier, previous work [3] involved piloted simulation of damage tolerant control laws using a simulated helicopter based on the Piasecki X-49A. In that study, a minimum landing speed of 60 kt was set since below that speed the redundant aerosurface controls could no longer be used [2, 23]. The full-scale minimum landing speed corresponds to 19 kt for the Scaled Demonstrator and therefore provides a good estimate of the minimum speed at which the aerosurfaces are sufficiently effective. This estimate of 19 kt is consistent with the results in Table 15 since the aerosurface responses were sufficiently effective for identification at 26 kt, but not at 13 kt.

Table 15. Control Redundancy

Virtual Effectors	Primary Aircraft Response by Flight Condition	
	Hover and 13 kt	26 and 39 kt
Lateral Cyclic (v_1)	Roll	
Longitudinal Cyclic (v_2)	Pitch	
Collective (v_3)	Vertical	
VTDP RPM (v_4)	Yaw	Forward Thrust
Rudder (v_5)	None	Yaw
Differential Flaperon (v_6)		Roll
Symmetric Flaperon (v_7)		Vertical
Elevator (v_8)		Pitch

Eigenvalue Trends with Airspeed

Figure 28 shows the trends of the linearized stitched model eigenvalues with airspeed. Each subsequent plot has increasing levels of zoom to highlight modes at lower frequencies. At each flight condition, there are eight modes (four lateral-directional, four longitudinal) with 12 eigenvalues total.

Starting at high frequency, the first two modes are the coupled lateral and longitudinal fuselage-rotor flapping modes, which correspond to the rotor flapping dynamics that were explicitly included in the hybrid model structure. The lateral flapping mode is stable (left-hand plane) and has a frequency and damping that *increase* from ($\omega_n = 36$ rad/s, $\zeta = 0.49$) at hover to ($\omega_n = 44$ rad/s, $\zeta = 0.69$) at 39 kt. Conversely, best seen from the second plot, the longitudinal flapping mode is stable and has a frequency and damping that *decrease* from ($\omega_n = 8$ rad/s, $\zeta = 0.98$) at hover to ($\omega_n = 6$ rad/s, $\zeta = 0.82$) at 39 kt.

The third mode is the VTDP RPM motor lag break frequency $\omega_{lag} = 9.68$ rad/s, which represents the lag associated with

speeding up and slowing down the VTDP propeller. The fourth mode is the heading integrator located at the origin.

At hover, the fifth and sixth modes are the vertical speed-damping derivative $Z_w = -0.21$ and yaw stability derivative $N_r = -1.26$, which set the break frequencies of the yaw and z-body axis velocity responses, respectively. At higher speeds, the vertical mode transitions to become a coupled pitch-roll subsidence mode, which is stable and increases in frequency to 13 rad/s at 39 kt. At higher speeds, the yaw mode decreases in frequency and becomes a stable spiral mode.

At hover, the seventh and eighth modes are the lateral and longitudinal phugoid modes. The lateral phugoid is a stable complex pair that increasing in frequency ($\omega_n = 1.5$ to 4 rad/s) and decreases in damping ($\zeta = 0.22$ to 0.11) with airspeed; it becomes the typical fixed-wing Dutch roll mode at high speed. As shown in the third plot, the longitudinal phugoid is an unstable complex pair at low speed, then transitions to consist of two real eigenvalues (one stable, one unstable) at high speed. At around 13 kt, the eigenvalues associated with the longitudinal phugoid mode are even farther into the right-half plane (and therefore more unstable) than at hover, which may have contributed to the challenges for system identification at 13 kt discussed earlier in the paper.

Frequency Response Trends with Airspeed

Figure 29 shows the on-axis frequency response trends of the linearized stitched model with airspeed for each virtual effector. The changes in the on-axis roll response p/v_1 and pitch response q/v_2 with airspeed reflect the transition from hovering dynamics to fixed-wing-like dynamics at higher speeds [6]. The changes are larger at low frequency and are associated with the lateral phugoid/Dutch roll and longitudinal phugoid modes. At high frequency, the p/v_1 response magnitude gradually and monotonically increases similar to fixed-wing aircraft [6]. As was shown in the hover system identification results section, the p/v_1 response at each airspeed exhibits the lateral rotor flapping mode, which shifts the frequency response magnitude up at high frequency and has a break frequency associated with the lateral rotor flap stiffness $L_{\beta_{1s}}$. The high-frequency magnitude of q/v_2 also increases slightly with airspeed.

The changes in the z-body axis velocity response to collective w/v_3 are also most noticeable at low frequency. At hover and 13 kt, the magnitude exhibits the characteristic k/s shape and associated -20 dB/decade roll-off across the full frequency range. This indicates that the response is largely decoupled from other axes and is well approximated by a first order transfer function with a break frequency associated with the vertical speed-damping derivative, which is $Z_w = -0.21$ at hover. At 26 and 39 kt, the heave and pitch modes become coupled, which is typical of fixed-wing aircraft and results in distortion of the magnitude curve at low frequency [6].

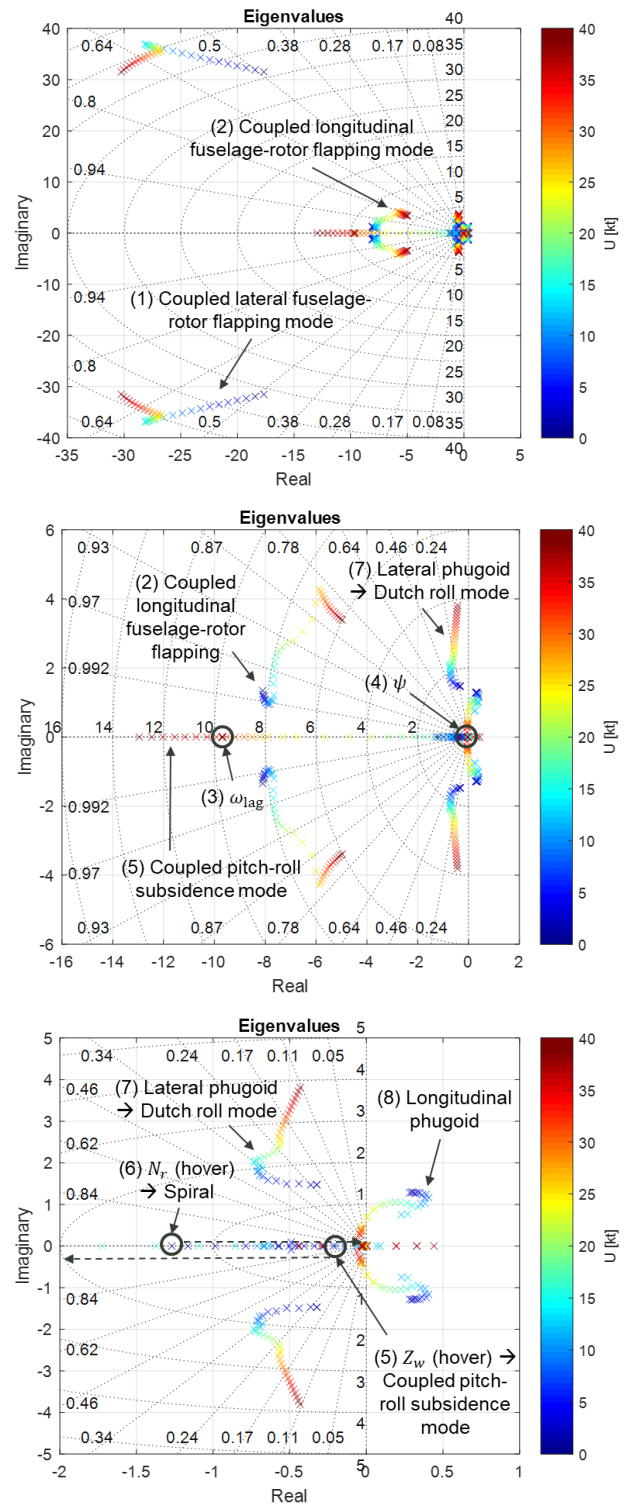
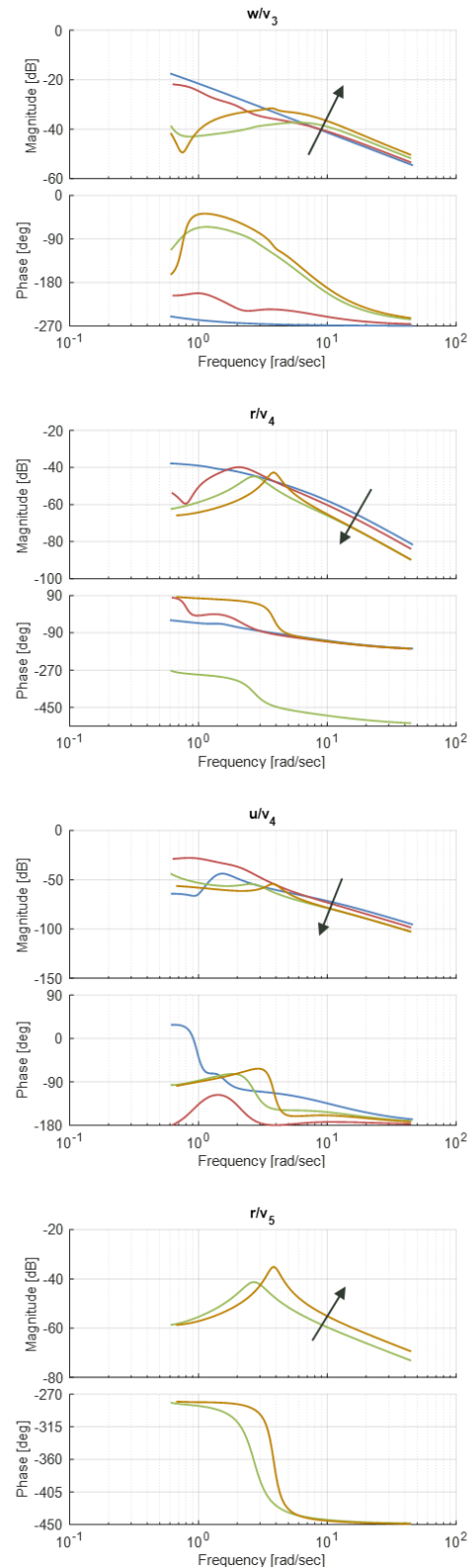
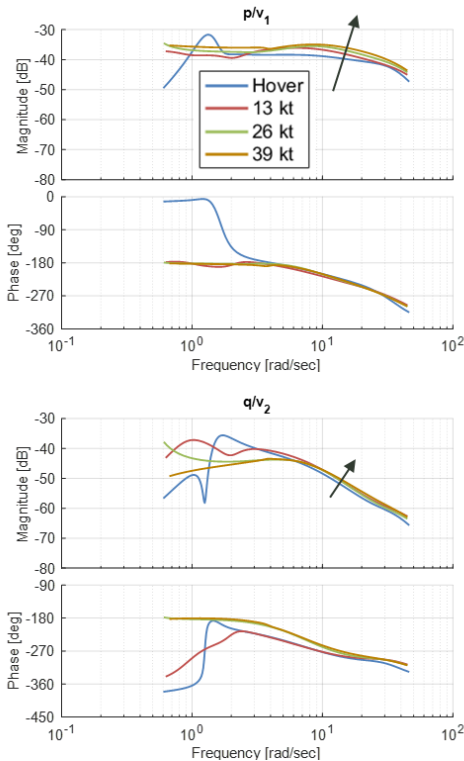


Figure 28. Linearized stitched model eigenvalue trends with airspeed. Each subsequent plot is zoomed in to highlight modes at higher, then lower frequency.

At hover, the yaw rate response to VTDP RPM r/v_4 similarly exhibits a k/s shape at high frequency with a break frequency associated with the yaw stability derivative $N_r = -1.26$. At high frequency, there is an additional -20 dB/decade roll-off (-40 dB/decade total) associated with the VTDP RPM lag break frequency at $\omega_{lag} = 9.68$ rad/s. At higher speeds, yaw and roll become coupled and form the Dutch roll mode, which results in distortion of the magnitude curve at low frequency. At high frequency, the magnitude progressively decreases due to the rotation of the VTDP sector, which directs airflow to provide yaw control at hover, and then forward thrust at higher speeds.

The x-body axis velocity response to VTDP RPM u/v_4 exhibits some distortion at low frequency due to the longitudinal phugoid mode. At high frequency, the response magnitude decreases with airspeed, due to the decrease in VTDP RPM trim setting from 0-26 kt (as shown in Figure 21). This comes from the relationship between thrust and RPM, which can be approximated as $T \propto RPM^2$ [21]. Thus, the control derivative varies as $\frac{\partial T}{\partial RPM} \propto RPM$ such that the ratio of forward thrust to RPM decreases as RPM decreases.

The on-axis responses to all the aerosurfaces – r/v_5 (yaw rate to rudder), p/v_6 (roll rate to differential flaperon), w/v_7 (z-body axis velocity to symmetric flaperon), and q/v_8 (pitch rate to elevator) – are only available at 26 and 39 kt where the aerosurfaces were sufficiently effective to identify responses. The magnitudes for all aerosurfaces responses increase with dynamic pressure and airspeed as expected. The r/v_5 response peaks at around 4 rad/s, which is indicative of the typical fixed-wing Dutch roll mode and consistent with the mode natural frequency shown in Figure 28 at higher speeds.



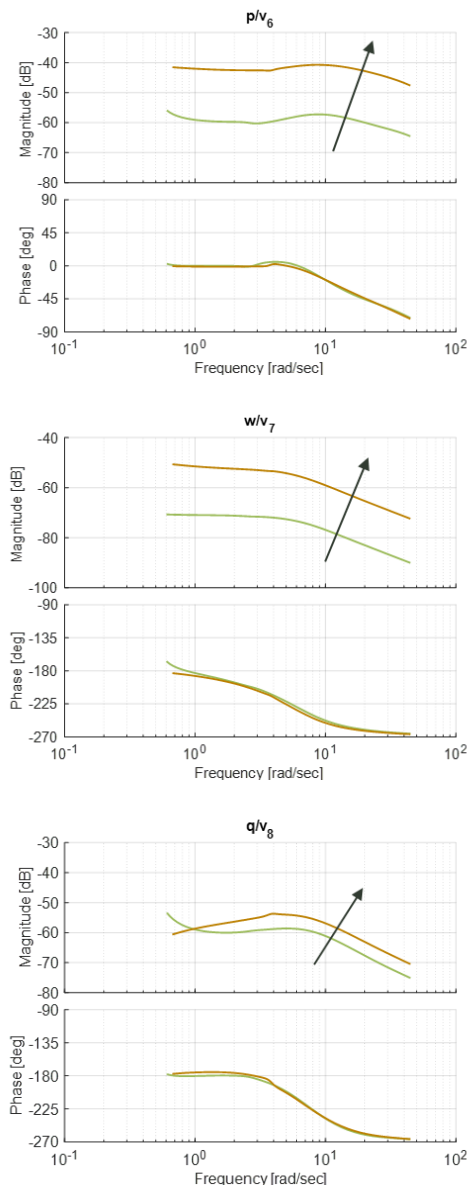


Figure 29. Linearized stitched model frequency response trends with airspeed.

LESSONS LEARNED

This section summarizes several key findings and lessons learned from this study involving the ADAPT™ Scaled Demonstrator, a 10% scale version of the Piasecki X-49A. These items may be useful to consider for system identification and full-envelope modeling and simulation of related subscale (and possibly even full-scale) aircraft. They are as follows:

1. A spacing of 13 kt (40 kt full scale) between point models and associated trim data was sufficient to produce a full flight envelope stitched simulation model. However, future work on aircraft with aerosurfaces should consider using a finer spacing near the flight condition at which the aerosurfaces become sufficiently effective to identify frequency responses. For example, for the Scaled

Demonstrator, an additional point model could have been obtained at around 19 kt. This would help improve the accuracy of identified aerosurface control derivatives at low airspeed where the signal-to-noise ratio and coherence is low. Additionally, since the VTDP sector is still partially rotated at around 19 kt, having an additional point model would help to accurately model the yaw and forward thrust responses to VTDP RPM at this flight condition.

2. Automated frequency sweeps producing roll, pitch, and yaw rates of ± 25 deg/s and heave accelerations of ± 3 m/s² (± 8 deg/s and ± 3 m/s² full scale, respectively) were found to be sufficient for system identification (provide sufficient signal-to-noise and produce good quality frequency responses) and are consistent with the full-scale guidelines in [6].
3. Due to its highly coupled flight dynamics and redundant control effectors, system identification of the Scaled Demonstrator required using the Joint-Input Output (JIO) Method in addition to the Direct Method. The JIO Method was able to accurately identify the aircraft response to each virtual effector, even in the presence of highly correlated secondary inputs. In cases where accurate frequency responses were available from both the Direct and JIO Methods, the response with the higher coherence was used for state-space identification.
4. As is common for single main rotor helicopters, in this study it was difficult to achieve satisfactory coherence at low frequency due to low signal-to-noise ratio and high cross-control correlations at low frequency. Although there was sufficient data to identify X_u with good precision, the speed-stability derivative M_u had a large insensitivity value. Therefore, M_u was calculated and fixed during state-space model identification. This also highlights the importance of static stability data at each flight condition, which were used to obtain trim gradients for the calculation of M_u .
5. Since sweeps directly into the actuators (rather than into the tracking commands) were required to excite the aerosurfaces, the aerosurface frequency responses had poor coherence, particularly at low frequency. Therefore, a two-part identification approach was successfully applied. First, only the stability derivatives (low frequency) and rotor, VTDP RPM, and rudder control derivatives and time delays (high frequency) were included in the model structure and identified using the rotor, VTDP RPM, and rudder frequency responses only. Next, the parameters identified in the first step were frozen and only the remaining aerosurface control derivatives and time delays (high frequency) were identified using all of the frequency responses. This method ensured that the highest quality data was used to determine the core set of parameters in the model, which

was then augmented to include the aerosurface parameters.

6. Trim-shot data [3] was not available for this study, but would be highly recommended for future work to improve the accuracy of trim data at intermediate airspeeds in the stitched model. This is particularly true for aircraft such as the Scaled Demonstrator that have large changes to the trim control positions (e.g. VTDP sector, RPM, symmetric flaperon) with airspeed.
7. A new method was used to calculate trim for the rotor flapping states, which were not measured, from the linearized stitched model u -derivatives. This provides physical understanding of the lateral and longitudinal rotor disc tilt with airspeed.

CONCLUSIONS

This study covered system identification and stitched modeling of the ADAPT™ Scaled Demonstrator winged compound helicopter. State-space models were identified at four flight conditions spanning the flight envelope with frequency- and time-domain costs meeting the guidelines, indicating very good agreement between the model and flight data. A full-envelope stitched model was developed from the point identification models and associated trim data. Trends of the stitched model trim, stability and control derivatives, frequency responses, and eigenvalues with airspeed were analyzed. The key findings of this study are as follows:

1. A combination of Direct and JIO Methods worked well to identify frequency responses for a highly coupled subscale winged compound helicopter with redundant effectors.
2. A hybrid model structure, which explicitly includes the fuselage-rotor flapping dynamics and a first-order VTDP RPM lag model, was required to accurately capture the system dynamics across the flight envelope. It resulted in low model mismatch costs in both the frequency and time domains.
3. Control redundancy exists for roll, pitch, and vertical responses at 26 and 39 kt. The redundancy provides the axes and airspeeds at which future work on damage tolerant control (DTC) will be done.
4. Key lessons learned from this study were summarized and provide useful guidance for system identification and full-envelope modeling and simulation of subscale and full-scale aircraft with redundant effectors. It was determined that finer spacing of point models and trim data would be advantageous at the transition airspeeds where the VTDP sector is rotating and the aerosurfaces are becoming sufficiently effective to identify.
5. A new method was developed to calculate trim for the rotor flapping states, which were not measured. The method relies on simultaneously solving for the trim

values at all flight conditions to minimize errors between the stitched model and identified u -derivatives. The updated trim resulted in physically reasonable trends and improved the match of the stitched model u -derivatives with those of the point models.

ACKNOWLEDGEMENTS

The authors would like to acknowledge the Piasecki flight-test team who was instrumental in collecting flight-test data used for system identification and stitched model development. Alex DiJoseph of Piasecki was the test pilot and provided useful observations of the aircraft behavior during flight testing. Eric Huang of Piasecki helped develop the control system and beep schedule used during flight testing and provided relevant information used in this study. Nic Kuhn provided test direction and planning, Steve Laughlin was vehicle crew chief, and Buz Conover and Fred Piasecki provided program management and guidance. Wael Shuaibi of Piasecki provided the aircraft CAD model inertias for use in the stitched model. Eric Tobias of DEVCOM AvMC provided support using the STITCH software tool. Anthony Gong of DEVCOM AvMC provided useful insights into using actuator commands [PWM] as the control inputs during system identification.

REFERENCES

1. "Adaptive Digital Automated Pilotage Technology (ADAPT™)," Piasecki Aircraft Corporation, <https://piasecki.com/projects/adaptive-digital-automated-pilotage-technology-adapt/2726/>. Accessed 17 Sep 2021.
2. Knapp, Marit E., Ivler, Christina, M., Horn, Joseph F., Johnson, Eric N., Bridges, Derek O., Lopez, Mark J. S., Tischler, Mark B., Wagster, Joseph A., Cheung, Kenny K., "Development and Simulation of Damage Tolerant Control Laws for a Compound Helicopter," AIAA SciTech, Orlando, FL, Jan 6-10, 2020.
3. Tobias, E. L. and Tischler, M. B., "A Model Stitching Architecture for Continuous Full Flight-Envelope Simulation of Fixed-Wing Aircraft and Rotorcraft from Discrete-Point Linear Models," U.S. Army AMRDEC Special Report RDMR-AF-16-01, April 2016.
4. Berger, T., Tischler, M. B., Knapp, M. E., and Lopez, M. S., "Identification of Multi-Input Systems in the Presence of Highly Correlated Inputs," AIAA SciTech, San Diego, CA, Jan 7-11, 2019.
5. Berger, T., Lopez, Mark J. S., Wagner, Aaron M., Tischler, Mark B., "Guidelines for System Identification of Multirotor Vehicles with Highly Correlated Inputs," Vertical Flight Society's 76th Annual Forum & Technology Display, Virginia Beach, VA, USA, Oct 6-8, 2020.
6. Tischler, M. B. and Remple, R. K., *Aircraft and Rotorcraft System Identification: Engineering Methods and Flight Test Examples Second Edition*, AIAA 2012.

7. Mettler, B., Tischler, M. B., and Kanade, T., "System Identification of Small-Sized Unmanned Helicopter Dynamics," Proceedings of the 55th Annual Forum of the American Helicopter Society, Montreal, Quebec, Canada, May 25–27, 1999.
8. Ivler, Christina M., Rowe, Elizabeth S., Martin, James, Lopez, Mark J. S., Tischler, Mark B., "System Identification Guidance for Multirotor Aircraft: Dynamic Scaling and Test Techniques," Journal of the American Helicopter Society 66, 022006 (2021).
9. Malpica, Carlos, "Handling Qualities Analysis of Blade Pitch and Rotor Speed Controlled eVTOL Quadrotor Concepts for Urban Air Mobility," presented at the VFS International Powered Lift Conference 2020, San Jose, CA, January 21–23, 2020.
10. Cheung, K., Wagster, J. A., Tischler, M. B., Ivler, C. M., Berrios, M. G., Berger, T., Juhasz, O., Tobias, E. L., Goerzen, C. L., Barone, P. S., Sanders, F. C., Lopez, M. J. S., Lehmann, R. M., "An Overview of the U.S. Army Aviation Development Directorate Quadrotor Guidance, Navigation, and Control Project," Proceedings of the 73rd Annual Forum of the American Helicopter Society, Fort Worth, TX, May 9-11, 2017.
11. Gong, A., Sanders, F., Hess, R., and Tischler, M. B., "System Identification and Full Flight-Envelope Model Stitching of a Package-Delivery Octocopter," Proceedings of the AIAA SciTech Forum, San Diego, CA, January 7–11, 2019.
12. Tobias, Eric L., Sanders, Frank C., Tischler, Mark B., "Full-Envelope Stitched Simulation Model of a Quadcopter Using STITCH," presented at the AHS International 74th Annual Forum & Technology Display, Phoenix, Arizona, USA, May 14–17, 2018.
13. Lopez, M. J. S., Duffy, C. S., Tischler, M. B., and Ruckel, P., "Bell V-280 Hover Flight Dynamics Model Validation and Update with Flight Test Data," presented at the Vertical flight Society's 77th Annual Forum & Technology Display, Virtual, May 10-14, 2021.
14. Berrigan, C. S., Lopez, M. J. S., Ruckel, P., and Prasad, J.V.R., "Bell V-280 System Identification and Model Validation with Flight Test Data using the Joint Input-Output Method", presented at the Vertical flight Society's 76th Annual Forum & Technology Display, Virtual, October 6-8, 2020.
15. Cheng, R. P., Tischler, M. B., and Schulein, G. J. (2006), "RMAX State-Space Helicopter Model Identification for Hover and Forward Flight," Journal of the American Helicopter Society, April, Vol. 51, No. 2, pp. 202–210.
16. Walker, J., Tischler, M. B., "Identification and Control Design of a Sub-Scale Flybarless Helicopter," presented at the Vertical Flight Society's 77th Annual Forum & Technology Display, Virtual, May 10-14, 2021.
17. Bhandari, S. and Colgren, R., "High-Order Flight Dynamics Models of a Small UAV Helicopter Using Analytical and Parameter Identification Techniques," Journal of the American Helicopter Society 60, 022012 (2015).
18. Marcos, A. and Balas, G. J., "Development of Linear-Parameter-Varying Models for Aircraft," AIAA Journal of Guidance, Control, and Dynamics, Vol. 27, No. 2, March-April 2004.
19. Berger, T., Tischler, M. B., Hagerott, S. G., Cotting, M. C., Gray, W. R., Gresham, J. L., George, J. E., Krogh, K. J., D'Argenio, A., Howland, J. D., "Development and Validation of a Flight-Identified Full-Envelope Business Jet Simulation Model Using a Stitching Architecture," AIAA SciTech Forum, Grapevine, TX, January 9-13, 2017.
20. Padfield, G. D., *Helicopter Flight Dynamics*, Wiley, 3rd ed., Hoboken, NJ.
21. Leishman, J. G., *Principles of Helicopter Aerodynamics*, Cambridge University Press, 2nd ed., New York, NY.
22. Berger, T., Juhasz, O., Lopez, M. J. S., Tischler, M. B., Horn, J. F., "Modeling and Control of Lift Offset Coaxial and Tiltrotor Rotorcraft," 44th European Rotorcraft Forum, Delft, The Netherlands, 19-20 September 2018.
23. Bridges, D. O., Berger, T., Horn, J. F., Hagwood, D. G., "Piloted Evaluation of Adaptive Flight Controls Designed to Improve Performance, Safety, and Survivability for Advanced VTOL Aircraft," presented at the VFS Modern Ops with Future Integrated VMS Technical Meeting, West Chester, PA, Aug. 19-20, 2021.